PHYSICAL REVIEW E **108**, 015301 (2023)

Dynamics of fluid bilayer vesicles: Soft meshes and robust curvature energy discretization

Ali Farnudi[*] and Mohammad Reza Ejtehadi
Department of Physics, Sharif University of Technology, P.O. Box 11155-9161, Tehran, Iran

Ralf Everaers
Ecole Normale Supérieure (ENS) de Lyon, CNRS, Laboratoire de Physique and Centre Blaise Pascal de l'ENS de Lyon, F-69342 Lyon, France

(Received 30 August 2022; revised 4 April 2023; accepted 26 May 2023; published 10 July 2023)

Continuum models like the Helfrich Hamiltonian are widely used to describe fluid bilayer vesicles. Here we study the molecular dynamics compatible dynamics of the vertices of two-dimensional meshes representing the bilayer, whose in-plane motion is only weakly constrained. We show (i) that Jülicher's discretization of the curvature energy offers vastly superior robustness for soft meshes compared to the commonly employed expression by Gommper and Kroll and (ii) that for sufficiently soft meshes, the typical behavior of fluid bilayer vesicles can emerge even if the mesh connectivity remains fixed throughout the simulations. In particular, soft meshes can accommodate large shape transformations, and the model can generate the typical ℓ^{-4} signal for the amplitude of surface undulation modes of nearly spherical vesicles all the way up to the longest wavelength modes. Furthermore, we compare results for Newtonian, Langevin, and Brownian dynamics simulations of the mesh vertices to demonstrate that the internal friction of the membrane model is negligible, making it suitable for studying the internal dynamics of vesicles via coupling to hydrodynamic solvers or particle-based solvent models.

DOI: 10.1103/PhysRevE.108.015301

I. INTRODUCTION

Lipid bilayers are an essential ingredient of the membranes surrounding cells, the basic structural and functional unit of most life forms [1,2]. Many fundamental processes such as shape transition, phase separation or budding can already be studied in vesicles formed by closed lipid bilayers [3–13]. For atomistic [14–20] or particle-based coarse-grain models of the bilayer structure and dynamics [21–29] molecular dynamics (MD) simulations are the method of choice. The employed software packages (for example, LAMMPS [30], GROMACS [31], and OpenMM [32]) allow the user to utilize preprogrammed potentials, integrators, thermostats, etc., and to perform calculations in parallel across multiple CPU and/or GPU platforms and high performance computing clusters.

When the thickness of the bilayer is very small compared to the length scale at which it is studied, it is convenient to represent it with a two-dimensional surface that has a stretch, shear, and curvature energy [4,33–37]. Such coarse-grained models are used to study vesicles as small as 100 nm up to a couple of tens of microns [7,38–41]. Shapes formed by simple membranes can be described quite well with bending energy [4] that is invariant under conformal shape transformations [42,43]. More complicated membranes, such as red blood cell membranes, require adding nonlinear area and shear strain to adequately describe their shape transitions [37].

Studying the dynamics of vesicles on the continuum level remains a theoretical [36,44–48] and computational [12,49–54] challenge. The present paper aims at developing a molecular dynamics compatible implementation of continuum models of fluid membranes, which faithfully represents the static properties of fluid bilayer vesicles and whose vacuum dynamics is nondissipative. In the future, we hope to couple our membrane model to explicit or implicit [55] models of the surrounding low Reynolds number medium, whose Stokes flow controls the dynamics of actual vesicles. Ultimately we are motivated by the idea of building a virtual cell model [56–58], which uses the molecular dynamics framework to integrate coarse-grained models of the various cell components into a unified model to mimic living cell behavior. Computational studies of continuum models of membranes use triangulated surfaces. While their elastic and bending energies can be rigorously defined [59–64], their evaluation is nontrivial. Two general methods are available to define a discretized bending curvature at a vertex on a triangulated lattice. In 1986, Itzykson [65] calculated an expression for the Laplacian of a scalar field on a triangulated lattice, assuming that vertices were homogeneously distributed and only connected to their first nearest neighbors (in other words, a surface tiled with acute triangles). A second method for discretizing the bending curvature on a triangulated lattice was introduced in 1996 by Jülicher [66]. Jülicher estimated the bending at each vertex by taking the average of the curvature of its surrounding triangle pairs. As demonstrated by Ramakrishnan *et al.* [67], this can be achieved by calculating the local curvature tensor of all the edges protruding from a vertex and projecting them on the tangential plane at the vertex.

Fluid membranes pose a particular challenge because they do not have a shear modulus. Dynamic triangulation [68,69],

---

[*] ali.farnudi@ens-lyon.fr

introduced in 1992, allows to adapt the mesh connectivity within a Monte Carlo (MC) simulation and relax shear forces while the surface continues to be tiled with triangles that have relatively the same area. Budding and phase separation of vesicles [70,71] and membrane tubulation [72] are just a few examples of many problems studied using dynamically triangulated network models [39,73,74]. While the technique can be combined with molecular dynamics simulations [40], it has the disadvantage that one frequently needs to "step" outside the MD environment and use meshing techniques to redefine the triangulated surface. This is also the issue when using MD to model surfaces as coarse-grained particles interacting using the Lenard-Jones (LJ) potential [75,76].

Unlike Itzykson, Jülicher made no particular assumptions concerning triangle shapes and sizes in deriving his expression for curvature. His method was probably not widely adopted because it offers no advantages for the hard meshes employed in conjunction with dynamic triangulation schemes. Here we show that Jülicher's method offers vastly superior robustness and stability for dynamical simulations of soft meshes with a more random distribution of vertices. In particular, we use this insensitivity of the curvature energy to the distribution of the vertices on the surface to perform molecular dynamics simulations of continuum models of fluid bilayer membranes, where the degrees of freedom are the vertices of a soft two-dimensional mesh with fixed triangular connectivity whose in-plane motion is only weakly constrained. The animations provided in the Supplemental Material [77] probably better convey the idea than a thousand words.

Our approach shares aspects with simulations that model vesicles with LJ particles, where particle coordinates can be used to reconstruct a triangular mesh to calculate the curvature energies [75]. Here we do not discretize the continuum model on a length scale comparable to the membrane thickness and as we treat the conservation of the membrane area globally and not locally, there is no coupling between the unresolved in-plane flow of lipids and the in-plane motion of the vertices of our soft mesh. Our approach shares with the fluctuating finite element analysis (FFEA) method [78] the interest in modeling fluctuating macromolecules or macromolecular assemblies on the mesoscale between atomistic or particle-based mildly coarse-grain models and finite-element descriptions of macroscopic matter. But while FFEA introduces thermal fluctuations into three-dimensional finite-element representations of macromolecules, we employ a molecular dynamics engine to simulate the standard continuum model of two-dimensional fluid bilayers.

The article is structured as follows. The theory section (Sec. II) summarizes the continuum theory of vesicle shapes and the statistical mechanics of triangulated surfaces before introducing mesh dynamics simulations as a method for simulating continuum models of fluid bilayer vesicles in a molecular dynamics framework. The Methods section (Sec. III) describes the implementation of mesh dynamics simulations into VCM and OpenMM, and provides details on the various sets of simulation runs. Our results are presented in Sec. IV. We establish the numerical foundations of mesh dynamics simulations (control of the mesh softness, precision, and robustness of different discretizations of the bending energy, time step, and stability) and present first quantitative and then qualitative validations of the method. In particular, we present a quantitative comparison of theoretical predictions for the excitation [45] and dynamical correlation of bending modes for nearly spherical vesicles to mesh dynamics simulation results for Newtonian, Langevin, and Brownian dynamics. Our results suggest (i) that despite the fixed mesh connectivity, the method can generate fluid behavior even for the longest wavelength bending modes and (ii) that the model's internal friction is negligible, making it suitable for studies of the internal dynamics of vesicles via coupling to particle-based solvent descriptions or hydrodynamic solvers. We discuss our findings in Sec. V before we present a summary and conclusions in Sec. VI.

To be complete while keeping the main article to a manageable length, we have consigned significant parts of the material to the Appendix and the Supplemental Material [77]. Appendix A summarizes the theory of surface undulations for nearly spherical vesicles, including our derivation of dynamical correlation functions for the Newtonian, Langevin, and Brownian dynamics of vertices. Appendix B provides the necessary theoretical background on the calculation of curvature energies for triangulated surfaces, while the Supplemental Material [77] contains details on the implemented many-body potentials. Finally, Appendix C contains a detailed discussion of the energy landscape surrounding individual vertices in mesh dynamics simulations as a means of understanding the origin of the superior robustness of curvature discretizations based on barycentric estimates of the plaquette area.

II. THEORY

To set the stage, we summarize in Sec. II A the continuum description of vesicle shapes, particularly Helfrich's spontaneous curvature model. Section II B briefly introduces the notion of surface modes for nearly spherical vesicles; details can be found in Appendix A. Section II C deals with the statistical mechanics of triangulated surfaces. We define meshes as being characterized by the positions and the connectivity of the vertices, discuss the calculation of the associated area, volume, and curvature energies (see Appendix B for details), define ensemble averages corresponding to the two types of disorder defining a mesh, introduce the notion of soft and hard meshes, as well as dynamic triangulation as the means of sampling different mesh connectivities. Finally, we introduce in Sec. II D mesh dynamics simulations as a complementary mesh adjustment method for simulating continuum models of fluid bilayer vesicles in a molecular dynamics framework that keeps the mesh's connectivity fixed and allows for variable triangle shapes and areas. We formulate the general mesh Hamiltonian, derive the resulting effective interactions and equations of motion, and justify the constant vertex mass approximation employed throughout the present work.

A. Continuum description

When the thickness of the membrane is very small compared to the length scale at which it is studied, it is convenient to represent it as a two-dimensional surface of a given area, A, which encompasses a certain volume, V. The local curvature energy density at each point of the surface is a function of the principle curvatures [79]. By definition, the two eigenvalues of the curvature tensor, C_1 and C_2, remain unchanged under coordinate rotation.

1. Area and volume

The surface $\mathcal{S}$ of a membrane is under tension, $\Sigma_{\rm st} = k_A\frac{A-A_0}{A_0}$, when the total area, A, is different from the equilibrium area, A_0 [13]. k_A denotes the compression modulus of the surface. The energy cost of changing the surface area of a membrane is described as the surface integral,

$$E_A(\mathcal{S}) = \int dA\, \Sigma_{\rm st} = \frac{1}{2}k_A\frac{(A-A_0)^2}{A_0}, \tag{1}$$

which is a quadratic function of the area difference.

For closed vesicles without holes, the energy cost of changing the enclosed volume is given by

$$E_V(\mathcal{S}) = \frac{1}{2}k_V\frac{(V-V_0)^2}{V_0}, \tag{2}$$

where k_V is the bulk compressibility and V_0 is the volume of the fluid enclosed by the vesicle [80].

2. Curvature energy

Helfrich described the curvature energy [4] using two independent bending moduli, the bending rigidity, κ, and the Gaussian curvature modulus, κ_G,

$$E_{\rm cur}(\mathcal{S}) = \int dA\left[\frac{1}{2}\kappa(C_1+C_2-C_0)^2 + \kappa_G C_1 C_2\right]. \tag{3}$$

Helfrich's bending energy also contains a characteristic curvature (or the spontaneous curvature), $C_0 = 2/r_s$, a function of the spontaneous curvature radius, r_s. In the case of most biological membranes, the chemical and protein composition of the enclosed fluid is different from the surrounding fluid. For example, proteins attached to the surface of a vesicle wall can induce a spontaneous curvature [81] and cause the lipid bilayer to favor bending toward the encapsulated fluid ($r_s > 0$) or the environment it is submerged in ($r_s < 0$).

Equation (3) is the sum of the bending energy, $E_b(\mathcal{S})$, and the Gaussian energy, $E_G(\mathcal{S})$,

$$E_b(\mathcal{S}) = \int dA\left[\frac{1}{2}\kappa(C_1+C_2-C_0)^2\right], \tag{4}$$

$$E_G(\mathcal{S}) = \textstyle\int dA[\kappa_G C_1 C_2]. \tag{5}$$

The bending energy, $E_b(\mathcal{S})$, describes the energy cost of local deviations from the spontaneous curvature due to thermal fluctuations and constraints imposed on the membrane. The Gaussian curvature energy, $E_G(\mathcal{S})$, describes the energy of saddle points and is calculated using the Gauss-Bonnet theorem [11]. The surface integral results in a constant determined by the genus (Euler characteristic), χ, of the surface,

$$\int dA\kappa_G C_1 C_2 = 4\pi\kappa_G(1-\chi). \tag{6}$$

χ counts the number of handles/holes in a closed geometry. For example, $\chi = 0$ for the surface of a sphere and $\chi = 1$ for the surface of a torus. Suppose we assume the membrane is a closed surface without tears and holes (and remains as such). In that case, the Gaussian energy will be equal to $4\pi\kappa_G$ for any deformation, including ones that originate from the area difference between the inner and outer leaflet of the bilayer [82]. Since the genus does not change for the vesicles considered in the present work, we can disregard $E_G(\mathcal{S})$.

3. Statistical mechanics

We are interested in the statistical mechanics of surfaces, $\mathcal{S}$, representing vesicle shapes. Expectation values of physical observables for vesicles are defined as ensemble averages over the all possible configurations of the vesicle surface,

$$\langle X\rangle = \frac{\int \mathcal{DS}\, X(\mathcal{S})\exp[-\beta E(\mathcal{S})]}{\int \mathcal{DS}\, \exp[-\beta E(\mathcal{S})]}, \tag{7}$$

where the energy $E(\mathcal{S})$ denotes the sum of the above area, volume, and bending energies.

B. Surface modes of nearly spherical vesicles

The properties of nearly spherical vesicles can be explored by expanding the surface undulations,

$$r(\theta,\phi) = r_0[1+g(\theta,\phi)], \tag{8}$$

into a sum of orthonormal modes,

$$g(\theta,\phi) = \sum_{\ell=0}^{\ell_{\max}}\sum_{m=-\ell}^{\ell} u_{\ell,m}Y_{\ell,m}(\theta,\phi), \tag{9}$$

where $Y_{\ell,m}(\theta,\phi)$ denotes spherical harmonics, Eq. (A3). In particular, one can calculate [34,44,45] the corresponding area [Eq. (A8)], volume [Eq. (A10)], and curvature energy [Eq. (A15)], from which Eqs. (A16) and (A17) for the mode fluctuation amplitudes, $\langle|u_{\ell,m}|^2\rangle$, follow via equipartition. In addition, we derive in Appendix the mode autocorrelation functions, $\langle u_{\ell,m}(t)u_{\ell,m}(0)\rangle$, for Newtonian, Langevin, and Brownian dynamics, Eqs. (A35), (A37), and (A39).

C. Statistical mechanics of triangulated surfaces

Numerical calculations for general shapes rely on the discretized representation of a surface via a mesh, $\mathcal{M}$, which is in turn defined by a connectivity graph, $\mathcal{G}$, and the vertex positions, $\boldsymbol{q} = \{\boldsymbol{q}_1, \boldsymbol{q}_2, \ldots, \boldsymbol{q}_N\} \in \mathcal{S}$. In particular, a vesicle shape can be triangulated by distributing vertices on the surface and connecting them. If the triangle edges defining the connectivity graph $\mathcal{G}$ are restricted to nearest-neighbor vertices, then the triangles tiling the surface will not overlap.

1. Two types of disorder

Triangulated surfaces can be categorized as ordered, random, fluctuating ordered, and fluctuating random meshes (Fig. 1). We define ordered meshes as triangulated surfaces with a highly regular distribution of vertices with the minimum possible number of degrees other than 6. For example, an ordered mesh on the surface of a perfect sphere can be triangulated with vertices with degree 6 and 12 vertices with degree 5 ($N_5 = 12$ and $N_7 = 0$). The locations of the vertices with degree 5 can be mapped on the corners of an Icosahedron [83].

Random meshes also have an almost homogeneous distribution of vertices on the surface, but they are populated with

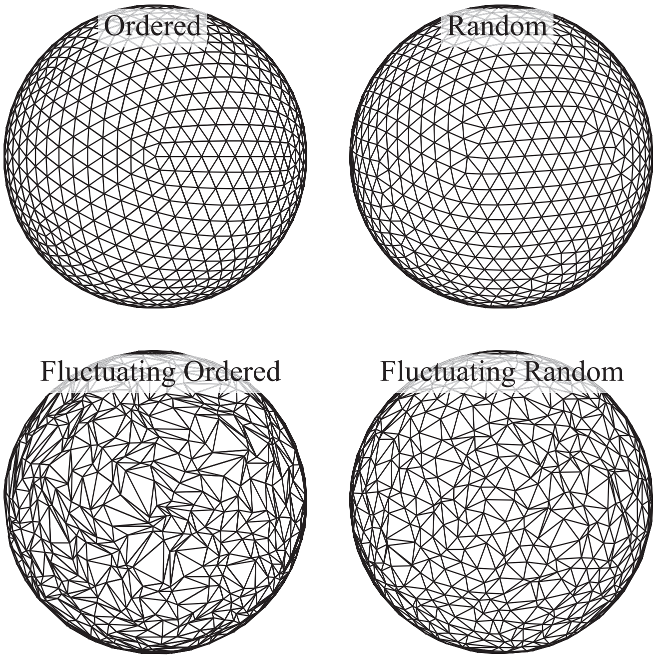

FIG. 1. Snapshots of the four different mesh types: Ordered (top left), random (top right), fluctuating ordered (bottom left), and fluctuating random (bottom right).

vertices with degrees 5,6,7,.... If the vertex distribution on the surface is nearly homogeneous, then one could limit the degree of vertices that appear at disclination and dislocation points to 5 and 7.

Fluctuating meshes can have an ordered or random connectivity but with an irregular vertex distribution. A configuration of mesh vertex coordinates is acceptable if (a) the triangles tiling the mesh surface do not overlap, and (b) a lower limit exists on the triangle area.

2. Area, volume and curvature energy of triangulated surfaces

In Appendix B, we summarize the calculation of the area, the enclosed volume, and the curvature energy of triangulated surfaces. As we have already stated in the Introduction, the calculation of the curvature energy is nontrivial. It can be discretized in terms of the mean curvature at each vertex $H_i = C_1 + C_2$, and the area associated with the vertex, a_i,

$$\begin{aligned} E_b &\equiv \frac{1}{2}\kappa \sum_i a_i [H_i - C_0]^2 \\ &= \frac{1}{2}\kappa \sum_i a_i \big[H_i^2 - 2H_i C_0 + C_0^2\big]. \end{aligned} \tag{10}$$

The two available formulas for the local mean curvature, Eq. (B7), due to Itzykson [65] and Gompper and Kroll [84], and Eq. (B11), due to Jülicher [66], express H_i as ratios of two different estimates of the plaquette curvature and two different estimates of the plaquette area. For our numerical tests, we have actually considered all four combinations of the curvature and area estimates, Eqs. (B10), (B13), (B15), and (B16). The relative merits of the Voronoi and the barycentric area estimate (Fig. 14) will play a prominent role in this work.

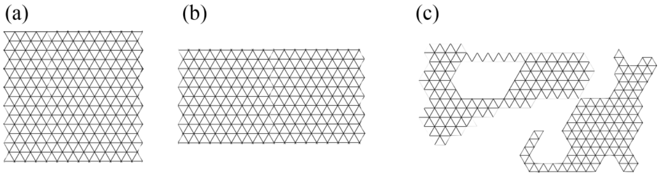

FIG. 2. Representation of (a) a regular square, (b) an elongated rectangle, and (c) two irregularly shaped surfaces of equal total area (340 triangles) via meshes containing equal numbers of equilateral triangles.

3. Ensemble averages

For discretized vesicles, ensemble averages over all possible configurations of the vesicle surface, Eq. (7), are replaced by corresponding traces over the mesh degrees of freedom,

$$\langle X \rangle = \frac{\sum_{\mathcal{G}} \int d\boldsymbol{q}\, X(\mathcal{G}, \boldsymbol{q}) \exp\left[-\beta U(\mathcal{G}, \boldsymbol{q})\right]}{\sum_{\mathcal{G}} \int d\boldsymbol{q}\, \exp\left[-\beta U(\mathcal{G}, \boldsymbol{q})\right]}, \tag{11}$$

where the energy

$$U(\mathcal{M}) = E(\mathcal{M}) + E_{\text{aux}}(\mathcal{M}) \tag{12}$$

of a mesh configuration $\mathcal{M} = (\mathcal{G}, \boldsymbol{q})$ is defined as the sum of (i) the sum of the discretized expressions for the area, volume, and bending energies of the represented surface, $\mathcal{S}(\mathcal{M})$, $E(\mathcal{M}) \approx E[\mathcal{S}(\mathcal{M})]$, and (ii) the sum of auxiliary potentials, $E_{\text{aux}}(\mathcal{M})$, controlling the triangle areas and shapes, bond lengths and angles, etc.

4. Hard versus soft meshes

The statistical weight of a mesh $\mathcal{M}(\mathcal{G}, \boldsymbol{q})$ representing a given surface $\mathcal{S}$ is given by

$$w(\mathcal{G}, \boldsymbol{q}|\mathcal{S}) = \exp\left[-\beta U(\mathcal{G}, \boldsymbol{q})\right] \prod_i \delta(\boldsymbol{q}_i \in \mathcal{S}). \tag{13}$$

In the equation above, $\delta(\boldsymbol{q}_i \in \mathcal{S})$ should be interpreted similarly to Dirac's δ, where meshes with coordinates at an appropriate distance with the surface are accepted. In the following, we refer to meshes as "hard," when the auxiliary potentials constrain the triangles to nearly uniform shapes and areas. Similarly, we refer to meshes as "soft," when said auxiliary potentials allow for a large variety of triangle shapes.

Most vesicle simulations employ hard meshes because the standard Gompper and Kroll discretization of the bending energy requires relatively regular triangulations. For a hard mesh, $\exp[-\beta E_{\text{aux}}(\mathcal{G}, \boldsymbol{q})]$ becomes vanishingly small for suboptimal tilings of a given surface $\mathcal{S}$. For example, a hard mesh in Fig. 2(a) needs to be rewired completely if the represented surface undergoes the area-conserving uniaxial elongation indicated in Fig. 2(b). As a consequence, simulations of dynamically evolving surfaces with hard meshes require frequent updates of the connectivity graph, $\mathcal{G}$.

For a soft mesh, realizations for a single connectivity graph $\mathcal{G}$ can represent a large variety of surfaces equally well. For example, the soft mesh representing the square in Fig. 3(a) can accommodate the uniaxial transformation of the rectangular shape in Fig. 3(b) by a simple affine transformation of the

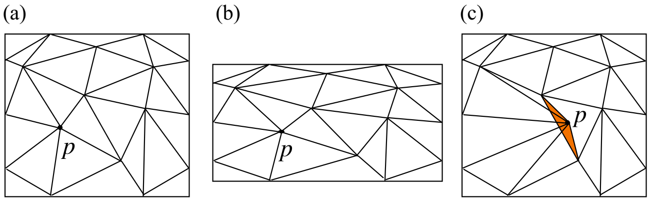

FIG. 3. Representation of (a) a regular square and (b) an elongated rectangle via meshes of equal connectivity and equal total triangle area. (c) Illustrates a square mesh with the same connectivity as (a) and (b) but a larger area due to an overlap of the orange triangle.

vertex positions. In particular,

$$\langle X\rangle \approx \langle X\rangle_{\mathcal{G}} = \frac{\int d\boldsymbol{q}\, X(\mathcal{G},\boldsymbol{q}) \exp\left[-\beta U(\mathcal{G},\boldsymbol{q})\right]}{\int d\boldsymbol{q}\, \exp\left[-\beta U(\mathcal{G},\boldsymbol{q})\right]}, \tag{14}$$

provided $\mathcal{G}$ is reasonably adapted to the shapes $\mathcal{S}$ with the largest statistical weights, $\exp[-\beta E(\mathcal{S})]$.

D. Simulating dynamically evolving meshes

1. Dynamic triangulation

The dynamic triangulation algorithm [68,69] allows to sample different mesh connectivities, $\mathcal{G}$, and is the most widely known and efficient remeshing technique used to represent vesicle surfaces. Generalizations [39] of the standard algorithm permit exploration of all possible shapes of a discretized two-dimensional fluid [Fig. 2(c)]. However, this generality comes at a price when the connectivity changes of a hard mesh are the main driver for shape evolution. Even a simple elongation [Figs. 2(a) and 2(b)] is slow and risks introducing dissipation into a dynamical scheme because it requires the local diffusive transport of triangles representing fixed amounts of bilayer area.

2. A molecular dynamics compatible mesh dynamics

As a complement to dynamic triangulation and the usual single vertex Monte Carlo moves, we propose to follow some of the earliest studies in the field [60,85,86] and to perform dynamical simulations of soft two-dimensional meshes with fixed triangular connectivity where the in-plane motion of the vertices is only weakly constrained. The idea is that individual vertices can move freely in 2D parallel to the surface under the condition [to be enforced via suitable auxiliary potentials, $E_{\text{aux}}(\mathcal{M})$] that the mesh cells tiling the surface do not overlap [Fig. 3(c)]. In general, the triangles or the plaquettes associated with individual vertices (Fig. 14) represent not a fixed amount of lipid bilayer but a fraction of the total mass corresponding to the ratio of the triangle or plaquette area and the (instantaneous) total area, $m_i = Ma_i/A$, which simplifies to $m_i \approx \rho a_i$ for a nearly constant total area. The collective vertex motion allows the mesh to dynamically evolve the surface, $\mathcal{S}$, in response to the stresses acting on it. In 3D, mesh dynamics simulations thus provide a semi-Lagrangian description of the evolution of curved surfaces. They are Lagrangian in the transverse direction (where the bilayer follows the motion of the mesh vertices), while the coupling between the in-plane dynamics and the flow of lipids depends on the auxiliary mesh potentials.

3. General Mesh Hamiltonian for variable vertex masses

As there is no coupling between the unresolved in-plane flow of lipids and the in-plane motion of the vertices of our soft mesh, the general expression for the Hamiltonian of the system is

$$\mathcal{H} = \frac{1}{2}\sum_{i}^{N} \frac{\boldsymbol{p}_i^2}{m_i(\boldsymbol{q})} + U(\boldsymbol{q}) \tag{15}$$

$$= \frac{A(\boldsymbol{q})}{2M}\sum_{i}^{N} \frac{\boldsymbol{p}_i^2}{a_i(\boldsymbol{q})} + U(\boldsymbol{q}) \tag{16}$$

$$\approx \frac{1}{2\rho}\sum_{i}^{N} \frac{\boldsymbol{p}_i^2}{a_i(\boldsymbol{q})} + U(\boldsymbol{q}), \tag{17}$$

where $\boldsymbol{p} = \{\boldsymbol{p}_1, \boldsymbol{p}_2, \dots, \boldsymbol{p}_N\}$ and $\boldsymbol{q} = \{\boldsymbol{q}_1, \boldsymbol{q}_2, \dots, \boldsymbol{q}_N\}$ denote the vertex momenta and positions, $m_i(\boldsymbol{q}) = Ma_i(\boldsymbol{q})/A(\boldsymbol{q})$ the vertex mass, $A(\boldsymbol{q})$ the instantaneous total area, and $U(\boldsymbol{q})$ the mesh potential energy including terms related to the total surface area, the enclosed volume, and the curvature energy.

4. Effective in-plane interactions between vertices

The conformation-dependent vertex inertia, $m_i(\boldsymbol{q})$, influences the vertex distribution on the surface. Integrating out the momenta, the statistical weight of a mesh configuration $\boldsymbol{q}$ is given by

$$\begin{aligned} w(\boldsymbol{q}) &= \exp\left[-\beta U(\boldsymbol{q})\right] \int d\boldsymbol{p} \exp\left(-\beta \frac{A(\boldsymbol{q})}{2M}\sum_{i=1}^{N}\frac{\boldsymbol{p}_i^2}{a_i(\boldsymbol{q})}\right) \\ &= \prod_{i=1}^{N}\left[\frac{2\pi M}{\beta}\frac{a_i(\boldsymbol{q})}{A(\boldsymbol{q})}\right]^{\frac{3}{2}} \exp\left[-\beta U(\boldsymbol{q})\right]. \end{aligned} \tag{18}$$

As expected, $w(\boldsymbol{q})$ is proportional to the Boltzmann weight $\exp[-\beta U(\boldsymbol{q})]$ related to the shape of the surface. The prefactor is maximal when all plaquettes have the same area, $a_i = A/N$, and can be rewritten in the form of a Boltzmann factor for an effective potential,

$$w(\boldsymbol{q}) = \exp\left[\frac{3}{2}\sum_{i=1}^{N}\log\left(\frac{2\pi M}{\beta}\frac{a_i(\boldsymbol{q})}{A(\boldsymbol{q})}\right) - \beta U(\boldsymbol{q})\right]. \tag{19}$$

To understand its effect, we focus on the deviations of the individual plaquette areas from the average, $a_i(\boldsymbol{q}) = A(\boldsymbol{q})/N + \delta_i(\boldsymbol{q})$:

$$\begin{aligned} \log\left(\frac{2\pi M}{\beta}\frac{a_i(\boldsymbol{q})}{A(\boldsymbol{q})}\right) &= \log\left(\frac{2\pi m}{\beta}\right) + \log\left(1 + \frac{N\delta_i(\boldsymbol{q})}{A(\boldsymbol{q})}\right) \\ &\approx \log\left(\frac{2\pi m}{\beta}\right) + \frac{N\delta_i(\boldsymbol{q})}{A(\boldsymbol{q})} - \frac{1}{2}\left(\frac{N\delta_i\boldsymbol{q})}{A(\boldsymbol{q})}\right)^2. \end{aligned}$$

Substituting this expression in Eq. (19), the sum of the zeroth-order terms is a constant, while the first-order terms add up to zero by definition. Retaining only the second-order terms,

$$w(\boldsymbol{q}) \propto \exp\left(-\beta\left\{\frac{3}{2}k_BT\sum_{i=1}^{N}\frac{1}{2}\left[\frac{N}{A_0}\delta_i(\boldsymbol{q})\right]^2 + U(\boldsymbol{q})\right\}\right), \tag{20}$$

we see that a harmonic potential restrains the plaquette areas to their average value.

5. General equations of motion

Neglecting the small variations in the total area, the general mesh equations of motion follow from Hamilton's equation of motion. From $\dot{\boldsymbol{q}}_i = \frac{\partial}{\partial \boldsymbol{p}_i}\mathcal{H}$ follows $\boldsymbol{p}_i = \rho a_i(\boldsymbol{q})\dot{\boldsymbol{q}}_i$. In a second step, $\frac{d}{dt}\boldsymbol{p}_i = -\frac{\partial}{\partial \boldsymbol{q}_i}\mathcal{H}$ implies

$$\frac{d}{dt}[\rho a_k(\boldsymbol{q})\dot{\boldsymbol{q}}_k] = -\frac{\partial U(\boldsymbol{q})}{\partial \boldsymbol{q}_k} - \frac{1}{2}\frac{\partial}{\partial \boldsymbol{q}_k}\sum_{i=1}^{N}\frac{\boldsymbol{p}_i^2}{\rho a_i(\boldsymbol{q})} \tag{21}$$

or

$$\rho a_k(\boldsymbol{q})\ddot{\boldsymbol{q}}_k = -\frac{\partial U(\boldsymbol{q})}{\partial \boldsymbol{q}_k} + \frac{1}{2}\rho\sum_{i=1}^{N}\dot{\boldsymbol{q}}_i{}^2\frac{\partial a_i(\boldsymbol{q})}{\partial \boldsymbol{q}_k} - \rho\dot{\boldsymbol{q}}_k\sum_{i=1}^{N}\frac{\partial a_k(\boldsymbol{q})}{\partial \boldsymbol{q}_i}\dot{\boldsymbol{q}}_i. \tag{22}$$

Solving these coupled equations of motion is challenging but, in principle, necessary to obtain the correct dynamics for systems like soap bubbles, where inertial effects are important and sensitive to the mass distribution on the triangulated surface.

6. Constant vertex mass approximation

Here we are interested in lipid bilayer vesicles in aqueous solutions, whose dynamics are controlled by the Stokes flow of the enclosed and the surrounding fluid [44,45]. In particular, inertial effects are irrelevant at low Reynolds numbers. We, therefore, study mesh dynamics in the much simpler constant vertex mass approximation,

$$\mathcal{H} = \frac{1}{2}\sum_{i}^{N}\frac{\boldsymbol{p}_i^2}{m_i} + U(\boldsymbol{q}), \tag{23}$$

where the standard Boltzmann weight gives the statistical weight of a mesh conformation,

$$w(\boldsymbol{q}) \propto \exp\left[-\beta U(\boldsymbol{q})\right], \tag{24}$$

and where the equations of motion reduce to Newton's equations of motion,

$$m_i\ddot{\boldsymbol{q}}_k = -\frac{\partial U(\boldsymbol{q})}{\partial \boldsymbol{q}_k}. \tag{25}$$

To improve the quality of the constant vertex mass approximation for the (vacuum) dynamics of a lipid bilayer with a nontrivial shape, one should either adjust the vertex masses to the average areas of the associated plaquettes, $m_i = \rho\langle a_i\rangle$, or employ a remeshing procedure to homogenize the plaquette sizes. But even in this case, the unphysically large fluctuations in the surface density inherent in mesh dynamics might have a detrimental effect.

III. METHODS

All presented simulations were carried out and can be reproduced using the virtual cell model (VCM) [56] software package that uses OpenMM MD engine [32] for running calculations in parallel on GPU and/or CPU platforms. VCM is open-source software, and the configuration files used to generate the presented data are available in the Supplemental Material [77].

A. Potentials and forces

OpenMM can automatically calculate the forces given expressions for the potential energy. This feature was crucial for the success of the present exploratory work since the explicit forms of the multiparticle (more than five particles) interactions for the area, volume, and bending energies derived in Supplemental Material Sec. II [77] are already intimidating enough by themselves. In addition to the physical potentials related to the vesicle shape, we have used two auxiliary potentials. The mesh softness is controlled via a WCA potential, U_h, on the triangle heights, h_j, given by Supplemental Material Eq. (8) [77], which sets a lower limit on the size of the plaquettes and ensures that vertices do not overlap with edges and other vertices. Furthermore, in rare occasions, it is useful to suppress large dihedral bending angles ϕ between adjacent triangles with an anharmonic $\mathcal{O}(\phi^4)$-bending potential (Supplemental Material Eq. (10) [77]).

B. Equations of motion

OpenMM's native Verlet integrator (leap-frog Verlet integration) was used to integrate Newton's equations of motion for a vesicle that evolves in a vacuum,

$$m_i\frac{d\vec{v}_i}{d_t} = \vec{f}_i. \tag{26}$$

For the study of vesicle fluctuations, OpenMM's Langevin integrator (LFMiddle discretization [87]) was used,

$$m_i\frac{d\vec{v}_i}{d_t} = \vec{f}_i - \gamma m_i\vec{v}_i + \vec{R}_i, \tag{27}$$

where γ is the friction coefficient, and $\vec{R}_i$ is an uncorrelated random force with a zero mean and values taken from a normal distribution with a variance, $2m_i\gamma k_BT$. Finally, for the high friction limit, OpenMM's Brownian Integrator was used to simulate systems where inertial forces can be ignored,

$$\gamma m_i\vec{v}_i = \vec{f}_i + \vec{R}_i. \tag{28}$$

C. Reduced units

VCM follows OpenMM's convention to set values for the units of m_0 (mass), l (length), ε (energy), and $\tau_{\mathrm{sim}} = \sqrt{m_0 l^2/\varepsilon}$ (time) in SI units (see Table I) where $k_BT = 2.49\varepsilon$ for $k_B = 8.3 \times 10^{-3}$ kJ/mol K and $T = 300$K. The choice of these numerical values does not affect the simulation results but makes

TABLE I. The adopted reduced units used in VCM and OpenMM.

Quantity	Units
l	nm
τ_{sim}	ps
m_0	amu
ε	kJ/mol

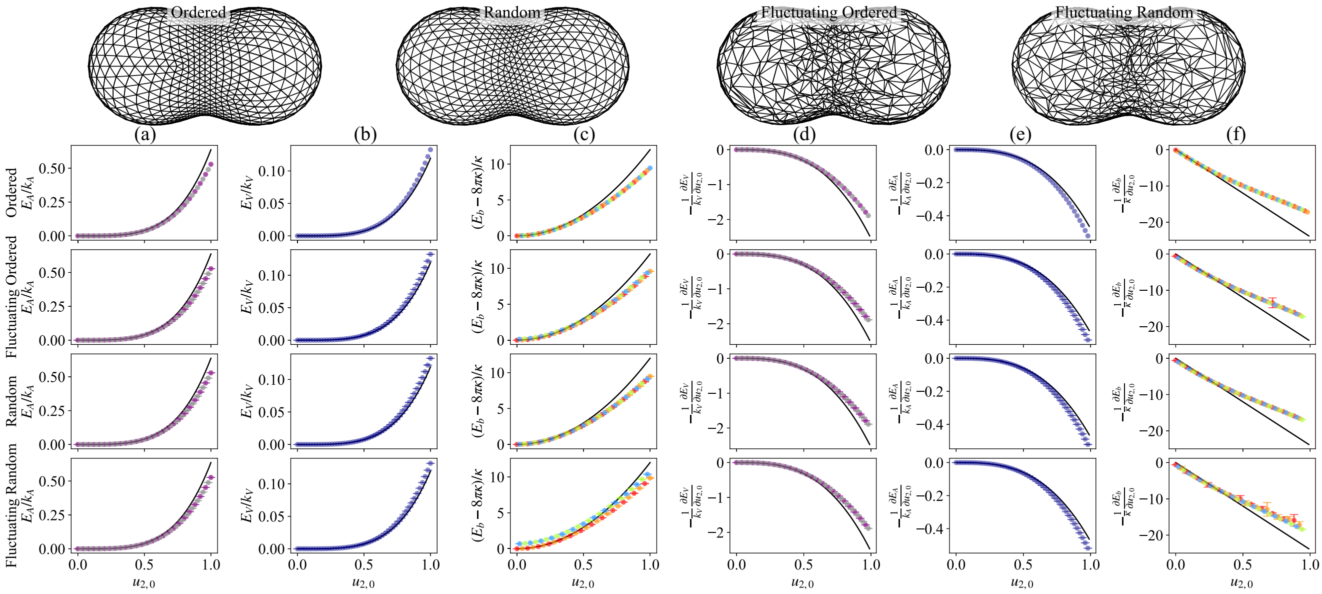

FIG. 4. Characteristics of deformed spherical surfaces for varying amplitudes of the mode $Y_{2,0}(\Omega)$.The snapshots show peanut-shaped meshes for the maximal considered amplitude of $u_{2,0} = 1$ generated by adding $Y_{2,0}(\Omega)$ to vertex coordinates for the different mesh types from Fig. 1. Columns (a), (b), and (c) plot the energy difference in the area, volume, and mean curvature. The surface energy is a function of the total surface of the mesh calculated by summing the Voronoi (purple) and Barycentric (gray) areas. The blue data show the volume energy calculated by summing the volume of the pyramids with triangle bases on the mesh surface. The black lines in columns (a) and (b) were generated using Eqs. (34) and (36). The curvature energy has the same color code as in Supplemental Material Fig. 6 [77]. The black line in column (c) plots Eq. (38), which correctly predicts the mean curvature energy for small amplitudes. The local slope of the energies corresponds to the restoring forces in mode space as a function of the mode amplitude for the area, volume, and mean curvature energy plotted in columns (d), (e), and (f). The black lines in these columns plot equations, Eq. (35), Eq. (37), and Eq. (39), respectively. The values are reported for meshes with (from top to bottom) an ordered, fluctuating ordered, random, and fluctuating random discretization. Error bars show the standard deviation from the mean.

converting experimental measurements to simulation parameters more convenient.

D. Simulation setup and default parameters

Detailed instructions on the preparation of the spherical meshes we have used as starting states and whose connectivity we have preserved throughout all presented simulations are provided in Supplemental Material Sec. III [77]. We typically set the initially enclosed volume and the initial mesh surface area to the ground-state volume V_0 (sum of the volume of triangular pyramids) and ground-state area A_0 (sum of the surface triangle area). The meshes used are publicly available in VCM's repository [56]. Typically, we use random triangulated meshes with radius $r_0 = 1000l$ and vertex mass $m = 50m_0$ to initiate the simulations. The default number of vertices is $N = 1002$, but meshes with $N = 252$, 492, 1962, and 4002 were also used when required. Our default values for the vesicle characteristics are

(i) an area compressibility $k_A = 5.22 \times 10^5 k_BT/r_0^2$ [88],

(ii) a bulk modulus $k_V = 1.6 \times 10^7 k_BT/r_0^3$ [88],

(iii) a bending rigidity of $\kappa = 20k_BT$.

E. Data acquisition

Unless stated otherwise,

(i) 10 mesh samples (N_{samples}) were used to obtain the values for each point.

(ii) The error bars show the standard deviation of the measured values divided by $\sqrt{N_{\text{samples}}} - 1$.

(iii) In case a Langevin integrator was used, the friction was set to $\gamma = 0.01\tau_{\text{sim}}^{-1}$.

(iv) Meshes were simulated with U_A, U_V, U_h, and one of the bending potentials U_b.

Fig. 4: Except for the ordered mesh that has a unique configuration for each mesh resolution, 50 mesh samples were used to calculate the observables (No MD simulation). All meshes had 9002 vertices.

Fig. 5: For each data point, five random meshes were simulated using a Verlet integrator.

Fig. 6: The mode amplitudes were obtained by running Langevin simulations for roughly $\sim 20\,\tau_{2,m}$.

Fig. 7: The shapes were obtained by running Langevin simulations of initially oblate ellipsoids with a reduced volume ν. For each ν, the simulation was initiated with a very soft mesh ($\Phi \approx 0.037$) and was run for roughly $40\tau_{2,0}$ to ensure equilibrium. The mesh hardness was then increased during 3 intervals to reach the target hardnesses: $0.037 \to 0.15$, $0.15 \to 0.33$, and finally $0.33 \to 0.59$. At each interval, the mesh hardness was gradually increased over roughly $20\tau_{2,m}$ by adjusting d_h in the U_h potential. After the target hardness was reached, the simulation was extended an additional $20\tau_{2,m}$ to make sure the mesh was well equilibrated. In total, the simulations was run for $160\tau_{2,m}$ ($40\tau_{2,m}$ in the beginning and $40\tau_{2,m}$ for each interval).

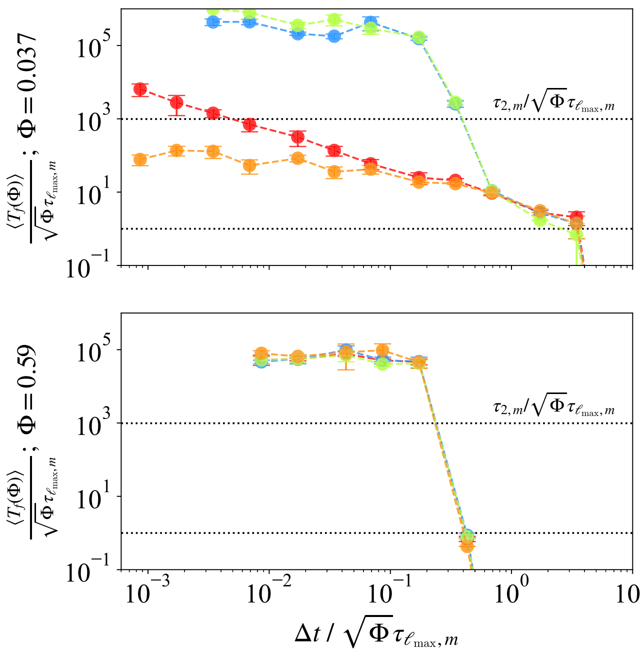

FIG. 5. The points show the average runtime before failure, $\langle T_f\rangle$, of simulations of a nearly spherical vesicle. The equations of motion were calculated using a velocity Verlet integrator until either the kinetic energy was doubled or the simulation failed due to numerical instabilities. The same color code as in Supplemental Material Fig. 6 [77] was used to indicate different bending models. $\epsilon = 4k_BT$, for the auxiliary potential U_h.

Figs. 9 and 10: The data was obtained by running five samples of random meshes for each regime. Each simulation was initially run for $\sim 20\tau_{2,m}$ using the Langevin integrator to obtain an equilibrated configuration. The equilibrated configurations were then extended for an additional $350\tau_{2,m}$ with a Verlet integrator with a short sampling rate ($2 \times 10^{-2}\,\tau_{7,m}$) to obtain trajectories suitable for autocorrelation calculations.

Fig. 11: Twenty samples were simulated with a Verlet integrator for each of the prolate and oblate ellipsoidal mesh's temporal bending energy evolution. All samples were initiated from a prolate or oblate soft mesh ($\Phi \approx 0.037$). The prolate ellipsoid with reduced volume $\nu = 0.4$ required an order of magnitude smaller time step to run stably.

IV. RESULTS

We begin by quantifying the softness of our meshes and exploring the relationship between their properties and our auxiliary potential for controlling the minimal triangle heights (Sec. IV A). In a second step, we explore in Sec. IV B the quality of discretized estimates of the vesicle area, volume, and curvature energy. In Sec. IV C, we define the time step for mesh dynamics simulations and explore their stability for different discretizations of the bending energy. Sec. IV E presents a quantitative analysis of the amplitude of surface undulations of nearly spherical vesicles, while Sec. IV F contains more qualitative results on the ability of soft meshes to accommodate larger shape changes. Finally, Sec. IV G presents a quantitative analysis of the dynamics of surface undulations of nearly spherical vesicles and some qualitative results for the timescale on which larger shape transformations occur. We close with some observations on the computational efficiency of the method and our implementation in Sec. IV H.

A. Soft meshes

In the first step, we need to define the meshes we will use to define vesicle shapes. Two distinct types of disorders characterize them. The disorder in the mesh connectivity (and hence the distinction between ordered and random meshes, see Supplemental Material Sec. III [77] for their construction on a sphere) remains unchanged or *quenched* in mesh dynamics simulations in the absence of additional connectivity altering operations like dynamic triangulation [68,69]. In contrast, the disorder in the shape and size of individual triangles is *annealed* since they constantly vary during mesh dynamics simulations. The amplitude of these fluctuations is controlled via the WCA-type auxiliary potential U_h (Supplemental Material Eq. (8) [77]), which controls the minimal triangle heights, h_j. It is important to note that in the absence of local strain energy affecting the triangle shapes, the definition of a buckling transition [89] will not apply. Consequently, disclination and dislocation points in the connectivity graph $\mathcal{G}$ do not perturb the represented surfaces.

1. *Mesh equilibration*

The **SM_AVh_V** movie in the Supplemental Material [77] shows a preview of the simulation output for a mesh running with U_A, U_V, and U_h (the "_AVh_" letters in the movie name indicate the use of these potentials). The details of the simulation setup and the parameters used are written in the Supplemental Material [77]. The simulation evolves with a Verlet integrator (indicated by the letter "_V" at the end of the movie name). The simulation time is measured in the WCA characteristic timescale, $\tau_h = d_h\sqrt{m/\epsilon_h}$, where m is the vertex mass. In the simulation, the vertices can move in space, and the mesh area and volume fluctuate around the mesh's initial respective values. Since in this simulation, we have not used a mean curvature potential, as long as the area and volume are maintained by U_A and U_V, triangle neighbors can make any angle without an energy cost. At the same time, area and volume potentials prevent the appearance of large spikes on the surface since they will change the reduced volume of the shape. A mean curvature model would be required to simulate a surface representing a vesicle, which will be discussed in the next section. Nevertheless, this system is a simple model to study the effect of applying dynamic area redistribution to a triangulated mesh. Supplemental Material Figs. 3 and 4 [77] show the corresponding temporal evolution of area size and bond length distribution. Mesh dynamics simulations are very fast in redistributing the vertices and quickly converge. Note that there is no appreciable difference between the distributions measured after $6.5\tau_h$ and $1100\tau_h$ (blue curve, nearly hidden in the background).

2. *Characterising and controlling the mesh softness*

The average shape of triangles that tile the surface of a mesh can be estimated by isosceles triangles with height, $\bar{h}$

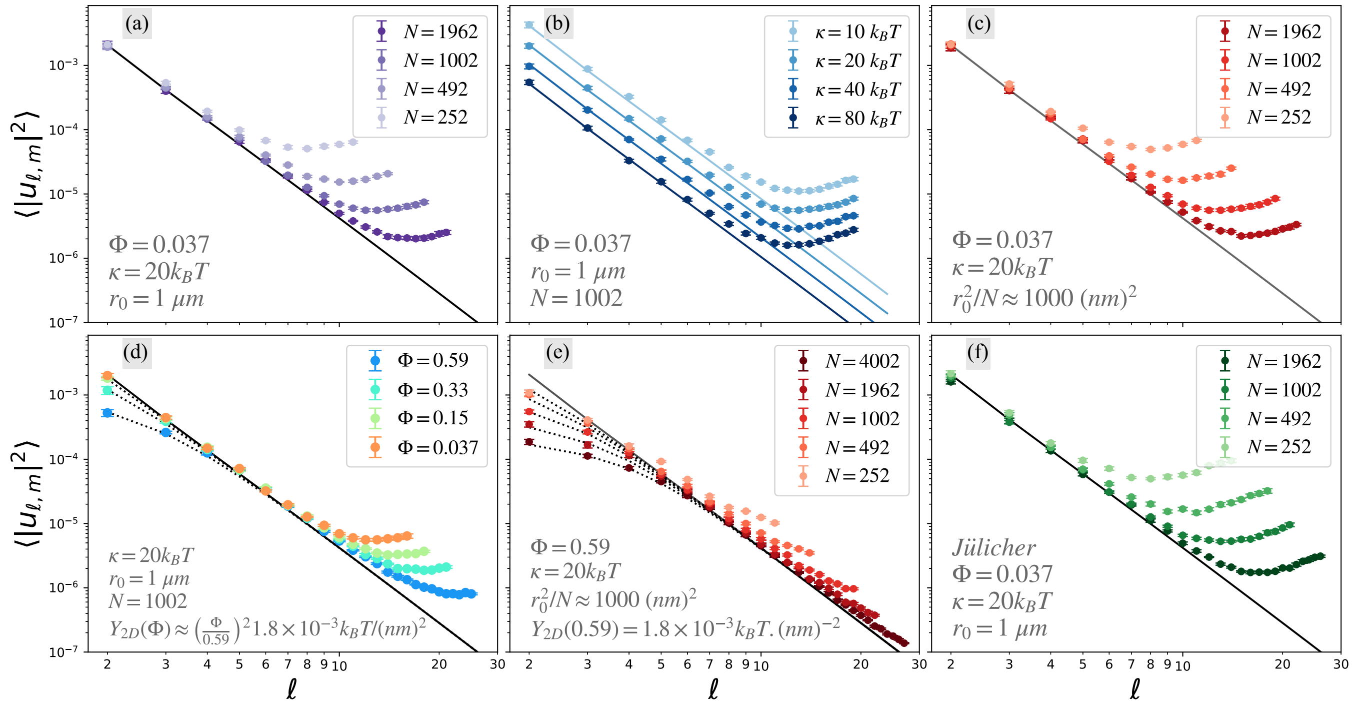

FIG. 6. Fluctuation amplitudes of spherical meshes as a function of spherical harmonics modes. All panels show data for systems without a volume potential ($P = 0$ or $k_V = 0$, respectively). (a) Vesicles, with radius $r_0 = 1$ μm, $\Phi = 0.037$, $\kappa = 20k_BT$, and different vertex numbers N. Meshes with a larger number of vertices can capture larger mode number deformations. (b) The fluctuation amplitudes decrease for meshes with the same $r_0 = 1$ μm, $\Phi = 0.037$, $N = 1002$, but higher bending rigidities κ. Panel (c) shows the independence of the fluctuation spectrum of vesicles from their size. (d) Meshes with $N = 1002$, $\kappa = 20k_BT$, but different Φ. A large Φ leads to solid-like behavior ($\sim\ell^0$) for small modes. The effective Young's modulus seems to follow $Y_{2D}(\Phi) = (\Phi/0.59)^2\, 1.8 \times 10^{-3}k_BT.(\mathrm{nm})^{-2}$. (e) A constant effective Young modulus for meshes with the same $\Phi = 0.59$ and bending modulus but different radii. (f) In this panel, we have reproduced the data presented in panel (a) using Jülicher's bending discretization with no visible difference in the vesicle spectrum. Solid lines plot the behavior described by Eq. (A17). All dashed lines plot Eq. (A18) for the provided inputs.

and the average area, $\bar{a}_{\text{iso}}$,

$$\bar{a}_{\text{iso}} = \frac{1}{\sqrt{3}}\bar{h}^2. \tag{29}$$

During dynamic area redistribution, the vertices are allowed to move on the surface. Hence a region may appear that is made from very small triangles. The area of these triangles, $\bar{a}_{\text{min}}$, are determined by the smallest height, d_h, allowed by the U_h potential,

$$\bar{a}_{\text{min}} = \frac{1}{\sqrt{3}}d_h^2. \tag{30}$$

As a simple measure of the admitted size fluctuations, we define the parameter

$$\Phi = \frac{\bar{a}_{\text{min}}}{\bar{a}_{\text{iso}}} = \left(\frac{d_h}{\bar{h}}\right)^2 \tag{31}$$

as the ratio of the smallest allowed and the average triangle area.

3. *Influence of Φ on the mesh properties*

Supplemental Material Fig. 5 [77] summarizes several results, which illustrate the influence of Φ on the behavior of our meshes. In Supplemental Material Fig. 5(a) [77] we show the amplitude of density modes $\rho_{\ell,m}$ inferred from the vertex positions on the surface of nearly spherical vesicles with reduced volume of $\nu = 1$. In analogy to the bending modes from Refs. [34,45] the density modes are defined in terms of spherical harmonics to account for the spherical geometry. For small values of Φ, the mode amplitudes for large ℓ approach the value of $\rho_{\ell,m} = 1$ characteristic of a two-dimensional ideal gas (black points) and indicative of the absence of structural order. A small effect of the connectivity of the vertices through the quenched triangulated network can be observed over large distances (small ℓ). In contrast, a marked peak appears around twice the maximum mode number ($\ell_{\text{max}} = \sqrt{N} - 1$) when $\Phi = \mathcal{O}(1)$. This coincides with a marked reduction in the fluctuations of the triangle areas (Supplemental Material Fig. 5(b) [77]) and a faster decay of the area autocorrelation function (Supplemental Material Fig. 5(c) [77]). This indicates the formation of a finitely compressible liquid-like mesh, where compression waves propagate more quickly. Such a mesh is not suitable for our purposes because it can probably not accommodate large deviations from the original shape.

B. Calculation of mesh observables

Before we can employ fluctuating ordered and fluctuating random meshes (see Fig. 1) for simulating vesicles, we need to ascertain that key observables like the vesicle area, volume,

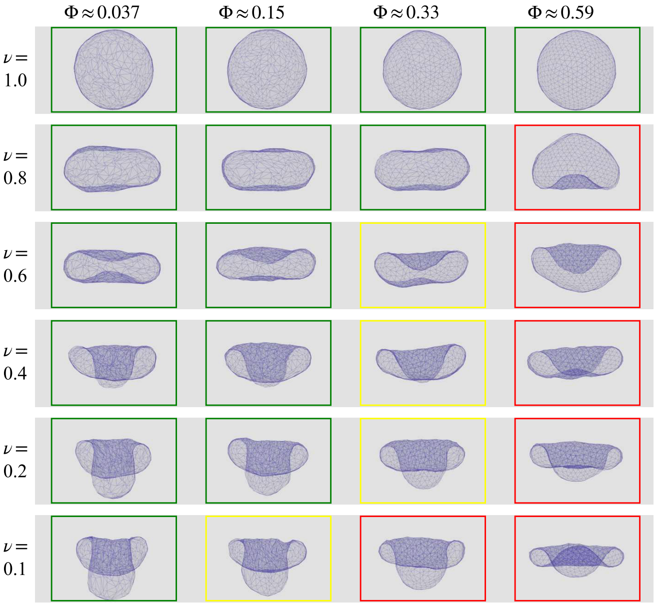

FIG. 7. Snapshots of fluid bilayer vesicle simulations using different combinations of ν and Φ. The area of the meshes was set to $A_0 = 4\pi(\mu\text{m})^2$ and $\kappa = 20k_BT$. Each row displays shape changes due to a gradual increase in the mesh triangle area ratio, $\Phi = 0.037$, adjusted through U_h. Shapes indicated with a green line are vesicle shapes that are compatible with the connectivity of the mesh. Yellow and red squares indicate meshes that require mild or frequent remeshing to produce the same shapes as their soft mesh counterparts.

and bending energy can be calculated with sufficient precision.

1. *Area and volume*

By mapping vertices of meshes on the surface of a unit sphere, the accuracy at which area and volume can be calculated was investigated as a function of mesh resolution. The results are presented in Supplemental Material Fig. 6 [77]. The total area of the meshes was calculated by summing the Voronoi (purple) and the Barycentric (gray) area of the vertices (left column), and the total volume (blue) of the meshes, calculated by summing over the tetrahedron volumes, is presented in the middle column. For all mesh types, the area and volume of a sphere can be calculated at very high accuracy, which improves with the resolution. A snapshot of each mesh type is placed next to each row as a visual guide for different mesh types.

The spherical meshes in Fig. 1 can be deformed by exciting spherical harmonic modes. This was achieved with the addition of a mode to the radial position of all vertices,

$$r(\theta, \phi) = r_0 + r_0|u_{2,0}|Y_{2,0}(\theta, \phi). \tag{32}$$

A peanut shape was generated by adding $Y_{2,0}(\theta, \phi)$ with amplitude $u_{2,0} = 1$ (top meshes in Fig. 4). The surface area energy of a deformed unit sphere was calculated by substituting

$$r(\theta, \phi) = r_0\left[1 + \sum u_{\ell,m}Y_{\ell,m}(\theta, \phi)\right] \tag{33}$$

in Eq. (1), and setting $\ell, m = 2, 0$,

$$E_A = \frac{2}{\pi}k_A|u_{2,0}|^4. \tag{34}$$

The retractive force as a function of the amplitude is

$$-\frac{\partial E_A}{\partial u_{2,0}} = -\frac{8}{\pi}k_A|u_{2,0}|^3. \tag{35}$$

Similarly, the energy cost of changing the volume of the unit to the peanut shape is calculated using Eq. (2),

$$E_V = \frac{3}{8\pi}k_V|u_{2,0}|^4, \tag{36}$$

and the opposing force is

$$-\frac{\partial E_V}{\partial u_{2,0}} = -\frac{3}{2\pi}k_V|u_{2,0}|^3. \tag{37}$$

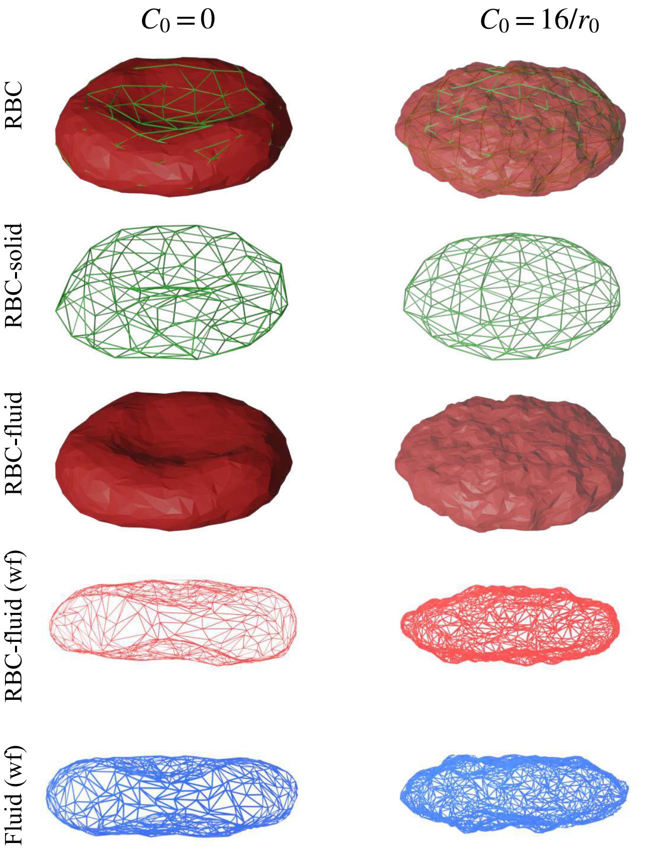

FIG. 8. Snapshots of RBC simulations where the spontaneous curvature of the fluid mesh was set to either $C_0 = 0$ (left column) or $C_0 = 16/r_0$ (right column). The RBCs have a diameter of approximately 2.6 μm, $\kappa = 50k_BT$, and the two-dimensional Young's modulus of the elastic (green) mesh was set to $Y_{2D} = 25$ μNm. The first row shows a snapshot of the composite mesh, while the second and third rows display the solid (green) and fluid (red) components separately. The last two rows compare a wire frame side view of the fluid part of an RBC membrane (composite mesh) with a vesicle (single fluid mesh) with the same properties. All green meshes have $N = 92$ vertices, and fluid meshes in the left column have $N = 1002$ vertices, whereas the ones in the right column have $N = 4002$.

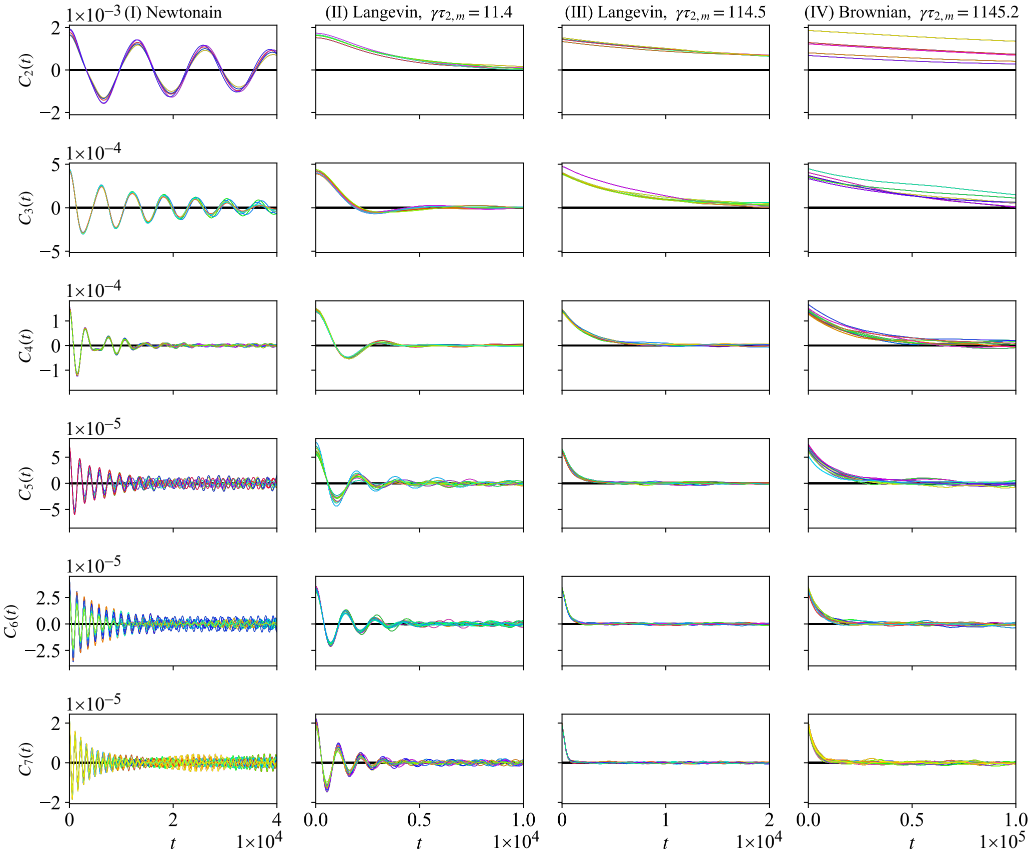

FIG. 9. The surface mode fluctuation amplitude autocorrelation for a vesicle with 1002 vertices and parameters reported in Sec. III D. The curves in the columns correspond to vesicles simulated using a Velocity Verlet (I), Langevin (II and III), and a Brownian (IV) integrator. Each curve corresponds to a different mode amplitude time series measurements identified by a random number seed (used to generate the mesh and initiate the random force generator) and the mode numbers ℓ and m. Column I has a sinusoidal form where each mode has a unique frequency. Columns II and III show underdamped and overdamped oscillations as a function of the oscillation frequency and integrator friction γ. Finally, column IV has exponential decay due to dominating friction forces.

In Fig. 4, columns (a) and (b), we have plotted the results for the changes in the area and volume energies due to the deformation of a mesh from a sphere ($u_{2,0} = 0$) to a peanut shape ($u_{2,0} = 1$). The local slopes of the area and volume energies are plotted in Fig. 4 columns (d) and (e) to approximate the restoring force applied to the surface vertices to pull them back to the surface of a sphere. The black lines draw the equations derived from mode analysis of "nearly" spherical shapes. For small deviations ($u_{2,0} < 0.5$), the measured values and the theoretical predictions correspond very well. The exponent of the energies and forces remain unchanged for large shape deviations, $u_{2,0} > 0.5$, and naturally, the values diverge. The data presented in Fig. 4 columns (a) and (d) emphasize that choosing Voronoi (purple) or Barycentric (gray) as the vertex area does not affect the energy and force calculations.

2. Curvature

The curvature energy of a unit sphere ($8\pi\kappa \approx 25.1\varepsilon$, $\kappa = 1\varepsilon$) can be calculated using Eq. (4) by substituting $C_1 = C_2 = \frac{1}{R}$, and $C_0 = \frac{2}{R_\infty} = 0$. The right column in Supplemental Material Fig. 6 [77] plots the normalized bending curvature energy of a unit sphere, calculated using four bending discretization models, Gompper&Kroll (red), Gompper&Kroll-Barycentric (blue), Jülicher (green), and Jülicher-Voronoi (orange) on regular and soft meshes with different resolutions.

It should be emphasized that any of the four models can be used to estimate the curvature energy of shapes for the different meshes. In the case of fluctuating random meshes, the curvature estimation becomes more precise as the resolution increases for models that use the Voronoi area (Gompper&Kroll and Jülicher-Voronoi), however, for models using the Barycentric area (Jülicher and Gompper&Kroll-Barycentric) the results deviate by ∼1.5% for our lowest resolution and asymptotically grows up to ∼4% as the number of vertices increases. This difference is due to the ratio of vertices with degrees N_5 and N_7 for different mesh resolutions and, consequently, the difference in the contribution of these vertices to the total bending (discussed in detail in Supplemental Material Sec. IV [77]). The effect of randomness in configuration (fluctuations) and topology can be compared by observing the second and last row in Supplemental Material Fig. 6 [77] right column. The fluctuating ordered meshes have the same mesh connectivity but random configurations, whereas the fluctuating random meshes are random both in topology and configuration. The curvature calculation models were initially derived for meshes with a homogeneous

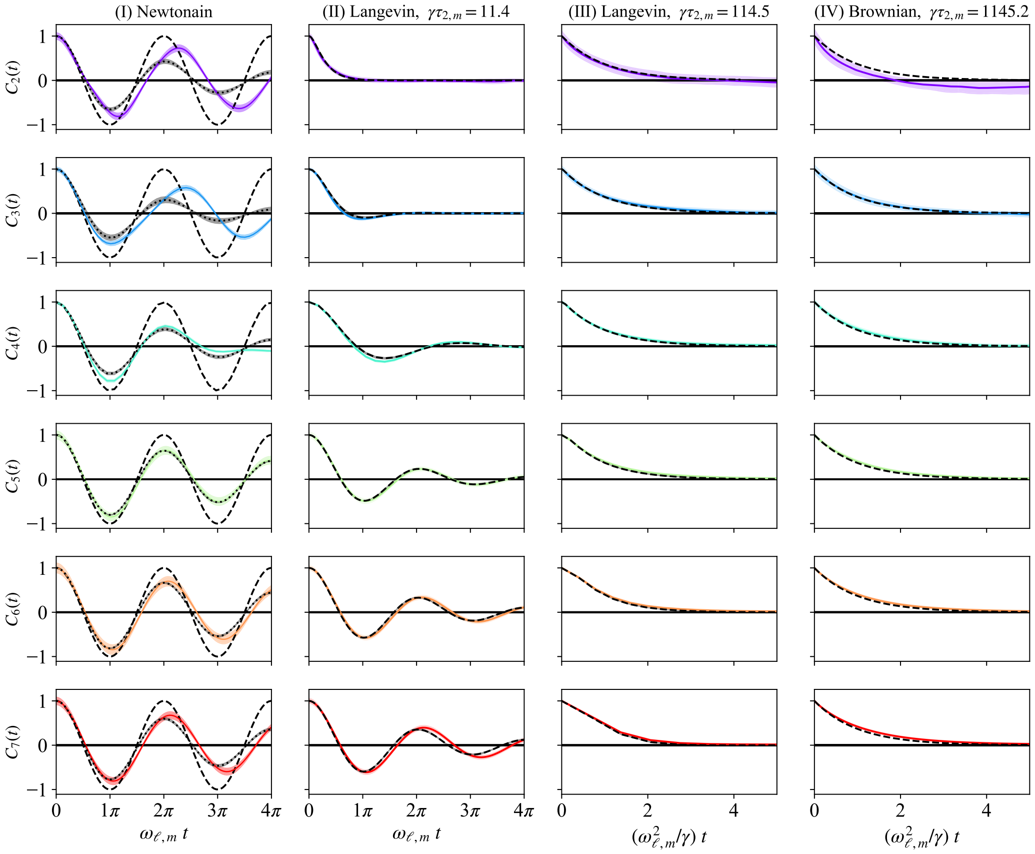

FIG. 10. The surface mode fluctuation amplitude autocorrelation for a vesicle with 1002 vertices and parameters reported in Sec. III D. The curves in the columns correspond to vesicles simulated using a Velocity Verlet (I), Langevin (II and III), and a Brownian (IV) integrator. The colored curves show the mean and standard deviation of the data presented in the respective column in Fig. 9. The black dashed lines plot $\cos(\omega_{\ell,m}t)$ for column I, the numeric results of Eq. (A35), Eq. (A36), or Eq. (A37) for the Langevin dynamics (columns II and III), and Eq. (A39) for the Brownian dynamics (column IV). The dotted lines in column I show a fitted curve representing underdamped dynamics used to measure the intrinsic friction, γ_ℓ.

vertex distribution. Hence, the curvature estimation for meshes with this property is very accurate. Our results show that these models produce reasonably accurate curvature estimation when used on fluctuating meshes. By increasing the resolution, we discover that randomness in topology affects the Barycentric-based models far more than the Voronoi-based models.

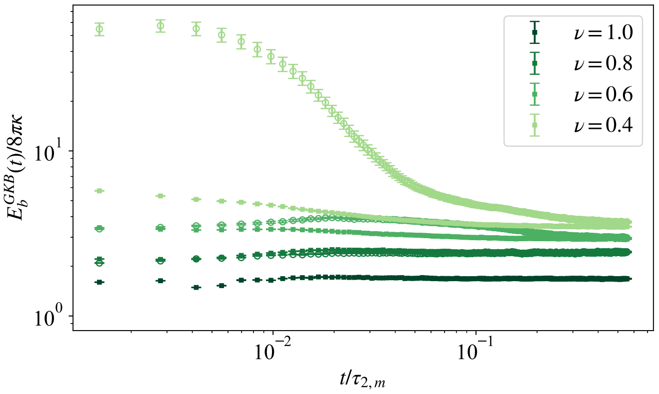

FIG. 11. The temporal evolution of the bending energy of oblate (filled symbols) and prolate (hollow symbols) ellipsoidal meshes with softness $\Phi \approx 0.037$.

In Fig. 4 column (c) the calculated curvature energy of meshes after adding a spherical harmonic mode with $\ell = 2$ and $m = 0$ with a range of amplitudes, $|u_{\ell,m}|$, between 0 (sphere) and 1 (peanut) was plotted. The curvature energy of a sphere deformed by a spherical harmonics mode and zero spontaneous curvature can be estimated for small deviations from a sphere [45],

$$E_b = 8\pi\kappa + 12\kappa|u_{2,0}|^2 \tag{38}$$

and the restoring force in mode space as

$$-\frac{\partial E_b}{\partial u_{2,0}} = -24\kappa|u_{2,0}|. \tag{39}$$

The discretized bending calculations [symbols in Fig. 4 column (c)] and predictions from Eq. (38) estimate the same curvature energy for small amplitudes ($|u_{\ell,m}| < 0.5$) and for larger amplitudes the two diverge since Eq. (38) was calculated for up to the quadratic term. Similar to the right column in Supplemental Material Fig. 6 [77], the four bending models calculate almost the same curvature for ordered and random meshes, and the curvature estimation difference for Barycentric and Voronoi-based models are also present in the peanut-shaped deformations for soft meshes (although very small for fluctuating ordered). Surprisingly all four models produce the same restoring force, which means that all of these models have the same shape dynamics, albeit the forces in the random and fluctuating meshes are slightly stronger compared to the ordered mesh [column (f) in Fig. 4]. In conclusion, if the topology of the mesh is not the major concern of the study, then fluctuating ordered meshes produce more precise absolute energy measurement and force calculation.

C. Mesh dynamics simulations

Having all elements in place to run actual mesh dynamics simulations, we start with some qualitative evidence that the method actually works. The movie **SM_AVh_GKB_V** shows the simulation preview of a soft mesh with U_A, U_V, U_h, and the Gompper&Kroll-Barycentric mean curvature potential, U_b^{GKB} that fluctuates in a vacuum. The simulation was initiated with a random mesh and a reduced volume, $\nu \simeq 1$. Because of the curvature potential, the mesh surface is smoother compared to the **SM_AVh_V** simulation that does not include a mean curvature potential.

In the following, we first show how to estimate a suitable time step for mesh dynamics simulations as a function of the vesicle and mesh characteristics. Then we test the stability of mesh dynamics simulations for the different discretizations of the bending energy.

1. Simulation time step

As the last step before running mesh dynamics simulations, we need to estimate the permissible time step, Δt. The in-plane motion of the vertices is limited by our WCA-like auxiliary potential, U_h, see Supplemental Material Eq. (8) [77] and Fig. 16(c1). In units of the bead mass, m, the minimal triangle height, d_h, and the energy scale, ϵ_h, of U_h the corresponding time is given by

$$\tau_h = d_h\sqrt{\frac{m}{\epsilon_h}}. \tag{40}$$

Alternatively we can use $4\pi r_0^2 \approx 2N\bar{a}_{\mathrm{iso}} = \frac{2}{\sqrt{3}}N\bar{h}^2 = \frac{2}{\sqrt{3}}\frac{N}{\Phi}d_h^2$ to express τ_h in units of the radius, r_0, and total mass, M, of the vesicle:

$$\tau_h = \sqrt{2\pi\sqrt{3}}\,\frac{\sqrt{\Phi}}{N}\sqrt{\frac{Mr_0^2}{\epsilon_h}}. \tag{41}$$

The transverse motion of the vertices is limited by the bending energy, U_b, see Supplemental Material Eqs. (4)–(7) [77] and the panels in the right-hand side (r.h.s.) column of Fig. 17. For a homogeneously tiled mesh, the oscillation time of the fastest bending mode is given by

$$\tau_{\ell_{\max},m} = \frac{2\pi}{N}\sqrt{\frac{Mr_0^2}{4\pi\kappa}} = \frac{1}{\sqrt{2\sqrt{3}}}\bar{h}\sqrt{\frac{m}{\kappa}}. \tag{42}$$

In soft meshes, regions may appear where all triangles have the smallest possible height d_h. Substituting d_h for $\bar{h}$ in the above expression, we estimate that the oscillation time of the central vertex in such small plaquettes is of the order of

$$\sqrt{\Phi}\tau_{\ell_{\max},m} = \frac{1}{\sqrt{2\sqrt{3}}}d_h\sqrt{\frac{m}{\kappa}} = \sqrt{\Phi}\frac{1}{N}\sqrt{\pi\frac{Mr_0^2}{\kappa}}. \tag{43}$$

The admissible time step is a fraction of the minimum of τ_h and $\sqrt{\Phi}\tau_{\ell_{\max},m}$. There are several ways of reading the above results. When expressed in microscopic units for given material parameters and vertex masses, we see that the time step for a given spatial resolution is independent of the size of the vesicles. Expressing the characteristic times in terms of the target vesicle's total mass and surface area reveals how the time step depends on the properties of the employed mesh. Not surprisingly, the time step is smaller for a finer spatial resolution with larger values of N. Choosing a small value of Φ to allow for large fluctuations in the triangle sizes also reduces the time step. Importantly, the choice

$$\epsilon_h < 2\sqrt{3}\,\kappa \tag{44}$$

for the energy scale of the auxiliary potential U_h assures that the time step of mesh dynamics simulations is limited by the physical bending rigidity independently of the mesh characteristics.

2. Stability of mesh dynamics simulations

To test the stability of mesh dynamics simulations and the influence of the discretization of the bending energy, Supplemental Material Eqs. (4)–(7) [77], we have run a series of simulations of this type for nearly spherical vesicles with properties described in Sec. III D. By setting $\epsilon_h = 4k_bT$ and $\kappa = 20k_BT$ we satisfy Eq. (44) and, accordingly, must set the simulation time step to a suitable fraction of the shortest bending timescale $\sqrt{\Phi}\tau_{\ell_{\max},m}$. With the choice of parameters used (see Sec. III D), the timescale for the in-plane motion of the vertices is $\tau_h \approx 45\tau_{\mathrm{sim}}$. Adjusting d_h to get a mesh with $\Phi = 0.037$, the out-of-plane shortest oscillation timescale of the vertices is $\sqrt{\Phi}\tau_{\ell_{\max},m} \approx 10.8\tau_{\mathrm{sim}}$. A suitable MD time step would correspond to roughly $\Delta t \sim 0.01\sqrt{\Phi}\tau_{\ell_{\max}}$. Starting from nearly spherical random meshes that initially have $\Phi \sim 1$ we measure the total simulation time T_f until the energy increases by 50% either due to a slow drift or a catastrophic failure.

In Fig. 5, we show for soft and hard meshes how the average simulation runtime to failure, $\langle T_f\rangle$ varies as a function of the time step, Δt. For hard meshes with $\Phi = 0.59$ mesh dynamics simulations can be stably run with time steps up to $\Delta t = \mathcal{O}(1/10)\sqrt{\Phi}\tau_{\ell_{\max},m}$. The unexpectedly large stability might be due to the harmonic character of the out-of-plane potential. In particular, the discretization scheme of the bending energy has no discernible influence on the stability. For soft meshes with $\Phi = 0.037$, the same observations continue to hold for discretization schemes like Jülicher's, which use the Barycentric plaquette area. In contrast, for Voronoi-based discretization schemes like the one by Gompper&Kroll, simulations rapidly fail even for time steps that are orders of magnitude smaller.

Clearly, these differences are not due to the different expressions for the plaquette curvatures but to the use of different definitions of the plaquette area for the normalization: Our "Gompper&Kroll-Barycentric" model is essentially as stable as Jülicher's original model, while our "Jülicher-Voronoi" model displays the same difficulties as the original Gompper&Kroll model. In Appendix C, we explore the energy landscape surrounding individual vertex, assuming that the rest of the mesh remains frozen. As expected, the analysis shows that vertices can move nearly freely within as well as above and below their plaquette. For Barycentric-based models, the energy rapidly increases when they leave this zone so that they will always be guided back should an MD time step lead them outside. In contrast, Voronoi-based discretizations of the bending energy create zones with large *negative* energies outside the plaquette zone. Importantly, some of these regions are located just on the edge of the plaquette zone where the Voronoi formula for the plaquette area changes sign. This suggests the existence of low-energy transition paths out of the plaquette zone that allow vertices to fall into one of these pitfalls and disrupt the MD simulation via the accompanying conversion of potential into kinetic energy. For harder meshes, the auxiliary potentials prevent these instabilities, and the difference between the two estimates of the plaquette area becomes as insignificant as suggested by Fig. 14. We cannot exclude that these instabilities could also be prevented for soft meshes through more salient choices for the auxiliary potentials. However, since the Barycentric models produce excellent results, we see at present no real motivation to pursue the development of MD methods based on Voronoi expressions.

D. Vesicle area

The area potential controls the surface area of a fluctuating vesicle through the surface compressibility, k_A [Eq. (1)]. The panels in Supplemental Material Fig. 7 [77] plot the ratio of the average area of simulated vesicles to the area of a sphere that has the same radius as the vesicle mesh. The data point corresponding to a vesicle simulated with $r_0 = 1$ μm, $\kappa = 20k_BT$, $\Phi = 0.037$, and $N = 1002$ is indicated with a red circle to act as a reference across different panels.

All results show that the area of the vesicle slightly fluctuates around an average area determined by the number of vertices on the mesh, as demonstrated with different numbers of vertices for vesicles with a radius $r_0 = 1$ μm [Supplemental Material Fig. 7(a) [77]] and vesicles with radii $r_0 = 0.5$, 0.7, 1, and 1.5 μm [Supplemental Material Fig. 7(c) [77]].

The average area of the vesicle was not affected by the simulated bending rigidities [Supplemental Material Fig. 7(b) [77]] but increased slightly for higher choices of Φ [Supplemental Material Fig. 7(d) [77]].

E. Fluctuations of nearly spherical vesicles

Having established how to run stable mesh dynamics simulations for arbitrary meshes, we can now start to test the utility of soft meshes. Is it really true that the behavior of *fluid* bilayers can emerge in simulations of meshes with *fixed* connectivity as suggested by Eq. (14)?

As a first quantitative test, we have simulated nearly spherical vesicles without spontaneous curvature, $C_0 = 0$ for a wide range of combinations of radius, bending rigidity, spatial resolution, and mesh softness. The movie **SM_Ah_GKB_L** shows an example of the fluctuating vesicle for the softest mesh used ($\Phi \approx 0.037$). The various panels of Fig. 6 analyze individual dependencies. All data are shown in a log-log representation, and most of our data sets display the expected key signature $\langle |u_{\ell,m}|^2\rangle \propto \frac{1}{\ell^4}$ from Eq. (A17) for the long-wavelength bending modes of vesicles with fluid membranes. Below we first explore the effect of the employed mesh's spatial resolution and the variation of physical parameters. Then we concentrate on the influence of the mesh softness.

1. *The effect of the spatial resolution of the employed mesh*

In Fig. 6(a), we have plotted fluctuation amplitudes for meshes with the same radius, bending rigidity, and softness, Φ but with different numbers of vertices, N. Reassuringly, the long wave-length modes $\langle |u_{\ell,m}|^2\rangle$ are not affected by this choice and fall on the "fluid" spectrum indicated by the solid black line [Eq. (A17)]. Furthermore, the finer the resolution of the mesh, the larger the wave number and the shorter the wavelength up to which the fluid regime extends.

2. *Influence of the bending rigidity*

Equation (A17) predicts that the fluctuation amplitudes of fluid bilayer vesicles should be inversely proportional to the bending rigidity of the bilayer, $\langle |u_{\ell,m}|^2\rangle \propto \frac{k_BT}{\kappa}$. When the bending rigidity increases, the surface becomes harder to bend, and the fluctuation amplitudes decrease. Figure 6(b) shows the fluctuation spectrum of a soft mesh with $N = 1002$ vertices with $\Phi = 0.037$ for different bending rigidity values. The simulated vesicles beautifully display the expected behavior.

3. *Irrelevance of the vesicle radius*

However, given the same bending rigidity, the fluctuations spectrum of fluid meshes are independent of their size, as the results presented in Fig. 6(c) confirm for simulated meshes with different radii. In Fig. 6(c), the meshes with vertex number $N = 252$, 496, 1002, and 1962 correspond to vesicles with radius $r_0 = 0.5$ μm, 0.7 μm, 1 μm, and 1.5 μm, respectively.

4. *The effect of the softness of the employed mesh*

In Fig. 6(d), we take random meshes for a given resolution ($N = 1002$) of our target vesicles with $r_0 = 1$ μm and simulate them at different softness values. Soft meshes have a small elasticity due to the U_h potential that prevents the vertices from crossing triangle edges during their in-plane motion. For very soft meshes ($\Phi \ll 1$), the elasticity effect due to the vertex-edge collision is well suppressed, but as Φ was increased, the meshes behave like elastic membranes. The spectrum of elastic (solid) membranes displays an elastic regime ($\sim\ell^0$) that dominates the large shape deformations (small modes) and transitions into a curvature regime ($\sim\ell^4$) that dominates the large as depicted by Eq. (A18). In Fig. 6(d), the spectrum of a low Φ mesh shows "fluid" behavior (on the black line), while for $\Phi \geqslant 0.15$, small modes are deflected, indicating a "solid" regime. The dotted lines plot the elastic shell fluctuation amplitudes for $\Delta p = 0$ and a guessed input value for Y_{2D} as a function of mesh softness, showing a clear agreement with the behavior described by Eq. (A18). We conjecture that a soft mesh's Young's modulus is a function of mesh softness,

$$Y_{2D}(\Phi) = \left(\frac{\Phi}{0.59}\right)^2 1.8 \times 10^{-3}\, k_BT/(\text{nm})^2. \qquad (45)$$

5. Independence of the effective Young's modulus from the vesicle size

The number of modes affected by the elastic regime depends on the size of the vesicle [Eq. (A18)]. In Fig. 6(e), we show the spectrum of vesicles with the same bending rigidity and mesh softness but different radii (the same area to vertex ratio r_0^2/N). The Young's modulus described by Eq. (45) was used to describe the spectrum of these vesicles using Eq. (A18) (dotted lines). The radius of the smallest mesh was 0.5 μm ($N = 252$), and the largest one was 1.5 μm ($N = 4002$). These results solidify the hypothesis on the dependency of the intrinsic Young's modulus on Φ and mark the choice for low Φ values essential for simulating fluid vesicles with soft meshes.

6. Different choice of mean curvature discretization

Finally, we compare results for the Gompper&Kroll-Barycenter discretization and Jülicher's original mean curvature discritization [66]. Since both potentials use barycentric weights, they can both be used to simulate vesicles. In Fig. 6(f), we plot the same system as presented in panels *a*, but by using Jülicher's mean curvature potential and observe the same "fluid" behavior.

F. Accommodation of larger shape changes

To further investigate the ability of meshes to represent shapes different from those for which their connectivity was optimized, we have explored how our spherical meshes fare in simulations (i) of fluid bilayer vesicles with significantly diminished reduced volume and (ii) of a composite membrane model for red blood cells.

1. Vesicles shapes for smaller reduced volumes

As a first challenge, we have explored how our spherical meshes adapt to significant reductions of their reduced volume from the original value of $\nu \approx 1$ down to $\nu = 0.1$.

To obtain results for our softest meshes with $\Phi = 0.037$, we have (i) affinely deformed spherical random meshes (Fig. 1) into oblate ellipsoids of the target volume and area in a procedure analogous to the one depicted in Fig. 4 and (ii) simulated the temporal evolution of these unstable shapes using Langevin dynamics. For harder meshes, simulations starting from the ellipsoidal initial shapes tended to become unstable. We have instead re-equilibrated the shapes obtained for $\Phi = 0.037$ for larger values of Φ using a "push-off"-like procedure to slowly increase d_h [90]. The resulting shapes are shown in Fig. 7. For intermediate values of ν, they resemble red blood cell discocytes, but they become unphysical for smaller ν since we have not included interactions to prevent the surface from intersecting itself. The conformations can be compared to corresponding results of energy minimizations from Refs. [91–94] modulo the fact that mesh dynamics simulations generate ensembles of finite temperature shapes, including thermal fluctuations (Ref. [95] conducts a detailed comparison between ground-state shapes generated using different mean curvature potentials). For our softest meshes, the agreement is excellent for all studied reduced volumes down to the smallest value of $\nu = 0.1$ (green frames in Fig. 7), demonstrating that a soft mesh can sustain important shape transformations with little or no need for remeshing. The use of a harder mesh has no effect for sufficiently large ν, but small or significant deviations (yellow and red frames in Fig. 7, respectively) appear the earlier, the larger the value of Φ and hence the mesh stiffness. As demonstrated by Supplemental Material Fig. 8 [77], the appearance of visible deviations coincides with measurable differences in the bending energy as well as an increase in the energy absorbed by the auxiliary potential controlling the triangle shapes relative to the spherical case.

2. Composite membrane models for red blood cells

As a second example of the versatility of soft meshes, Fig. 8 shows results of mesh dynamics simulations of a composite membrane model for red blood cells [12,40]. The connectivity of the mesh representing the fluid cell membrane was adapted to nearly spherical shapes. The fluid mesh was set up with an area and volume potential and a mean curvature potential with bending rigidity of $\kappa = 50k_BT$. However, we now allow a nonvanishing spontaneous curvature C_0 of the fluid bilayer, Eq. (4). Moreover, the mesh representing the bilayer is coupled to a second mesh with a two-dimensional Young's modulus of $Y_{2D} = 25$ μNm [12,40], which represents the spectrin network and provides a strong elastic response to deformations. We have started our simulations from oblate shapes with a reduced volume $\nu = 0.6$. The results shown in the two columns of Fig. 8 are for RBC with spontaneous curvatures of $C_0 = 0$ and $C_0 = 16/r_0$, respectively. The two movies **SM_RBC_C0** and **SM_RBC_C0.006** animate both of the simulations of the RBC from the initial frame. They show the RBCs from different angles and also highlight the dynamics of the fluid and solid mesh (green). The first three rows show RBC composite meshes alongside separate views of the solid and soft meshes.

Finally, in the last two rows of Fig. 8, we present side views of the meshes representing the fluid bilayer of the RBC and of a corresponding vesicle without the spectrin layer (blue). Most of the shape properties of the RBC originate from the fluid properties of the mesh and not the elastic mesh. This can also be visually confirmed by watching the movie **SM_AVh_GKB_L_nu0.6** that shows the simulation output for a fluid vesicle with the same properties as the RBC with zero spontaneous curvature from different angles. For Stomatocyte and echinocyte shape transformations, one should use the area difference elasticity model (ADE), where the solid mesh will greatly contribute to the RBC shape [37].

G. Vesicle dynamics

To quantitatively characterize the vesicle dynamics in mesh dynamics simulations, we have measured the autocorrelation functions of the surface modes of nearly spherical vesicles. We have investigated three different types of equations of motion for the mesh vertices (Newtonian/molecular dynamics, Langevin dynamics, and Brownian dynamics), which OpenMM can easily generate, and for which we have derived theoretical expressions for the autocorrelation functions in Sec. A 6. We close our exploration of soft meshes and mesh dynamics simulations of continuum models of fluid bilayers by exploring the timescale on which the larger shape changes discussed in Sec. IV F occur in the present setup.

1. Fluctuations of nearly spherical vesicles

Figure 9 summarizes our raw data for vesicles with $\kappa = 20k_BT$ and a radius of $r_0 = 1$ μm represented by a soft mesh ($\Phi = 0.037$) with $N = 1002$ vertices. Results for Newtonian dynamics, Langevin dynamics with two different levels of damping ($\gamma = 0.001$ and $\gamma = 0.01$), and Brownian dynamics are shown in this order in separate columns. Although inertia does not exist in the Brownian equation (mass is zero), γ can be calculated by dividing the Brownian friction ζ by the vesicle mass used in the simulations to compare the results in a similar format as the Langevin columns.

Panels in a particular row show results for a common mode number, $\ell \in [2, 7]$. The individual curves represent time averages for individual modes (ℓ, m) from five independent runs. Since there are $2\ell + 1$ independent values of m for a given mode number ℓ, there are more curves for larger mode numbers; for example, we have plotted 25 curves for $C_2(t)$ and 75 for $C_7(t)$ in column I.

Qualitatively, the data shown in Fig. 9 are relatively easy to interpret. For Brownian dynamics and Langevin dynamics with the higher friction value of $\gamma = 0.01$ all shown modes are overdamped. For Langevin dynamics with $\gamma = 0.001$ only the $\ell = 2$ mode is overdamped, the $\ell = 3$ mode is close to critical damping, while modes with $\ell \geqslant 4$ are underdamped. For Newtonian/molecular dynamics, all modes are underdamped.

For a quantitative analysis, we compare in Fig. 10 the respective ensemble averages of the data from Fig. 9 to the theoretically expected correlation functions derived in Appendix A 6. In contrast to Fig. 9, we no longer plot all data on a common time axis but rescale time with ℓ-dependent damping or oscillations times.

For Newtonian dynamics (i.e., a vesicle that oscillates in a vacuum), Eq. (A30) suggest that surface modes should oscillate stably and hence have a sinusoidal autocorrelation function. Instead, we observe a weak damping, that we ascribe to a Fermi-Pasta-Ulam-like dynamic coupling [96] between the modes due to the nonlinear auxiliary potential. Interestingly, the correlation functions for different ℓ look quite similar when plotted as a function of $\omega_{\ell,m} t$ (l.h.s. column of Fig. 10), suggesting that the intrinsic damping time of the modes is a faction of their oscillation time. This is confirmed by the fitted values for γ_ℓ for vesicles with different Φ values, which we have plotted in Supplemental Material Fig. 9 [77]. For soft meshes with $\Phi \ll 1$ we find $\gamma_\ell \approx 0.15\omega_{\ell,m}$ independently of ℓ. The intrinsic friction is larger for stiffer meshes with $\Phi = \mathcal{O}(1)$ without ever dominating the inertial dynamics.

We note that apart from the weak damping, the proper large-scale *inertial* dynamics emerges, even though our present implementation associates a constant mass to vertices independently of the variable surface area they represent. In principle, this is easy to correct. However, for efficiency reasons, the correction of the forces should be carried out within OpenMM. In practice, our understanding of the inner workings of OpenMM turned out to be too limited to implement a correction based on the user-defined barycentric plaquette areas in the heart of OpenMM's time step routine. While this can hopefully be corrected in future versions, we note that inertial effects play no role at the low Reynolds numbers relevant to the dynamics of vesicles or biological cells.

The surface undulations of vesicles in nature are highly damped and dominated by the hydrodynamics of the surrounding and enclosed fluids [44,45]. The negligible internal friction in undulations simulations is thus essential for the possibility of generating realistic dynamics in simulations where the present membrane model is coupled to hydrodynamic solvers or explicit (coarse-grain) solvent models. As a simple example, consider the above simulations with Langevin or Brownian dynamics, which couple the membrane motion to a viscous background.

In column II the data is also rescaled by the angular frequency of a harmonic oscillator $\omega_{\ell,m}$ for comparison with column I. $\omega'_{\ell,m}$ was theoretically calculated for columns II and III using the same input parameters used to set up the simulations (γ, κ, M, and r_0). Depending on the value of $\omega'_{\ell,m}$, one of the equations (A35), (A36), or (A37) was selected and plotted with black dashed line as the predicted oscillation. The error in fitting the equations was used to draw a gray area to indicate the error in plotting the theoretical calculations. Substituting the simulation parameters, we calculated $\ell_{\text{crit}} \approx 2.11$ ($\approx$2.26 if $\gamma_{\ell=2} \approx 0.00015$ is also considered) for column II, predicting that the slowest mode ($\ell = 2$) goes through overdamped oscillations and $\ell > 2$ go through underdamped oscillations. The same calculation places $\ell_{\text{crit}} \approx 6.68$ ($\approx$7.05 with $\gamma_{\ell=7} \approx 0.0011$) for column III. The theoretical curves confirm (with excellent precision) the observed transition from overdamped to underdamped for $\gamma = 0.001$ and the overdamped oscillation for the larger choice of thermostat friction ($\gamma = 0.01$).

The dashed black line in the final column was plotted using Eq. (A39). In the Brownian regimes, all modes decay at the same rate. This point was emphasized by rescaling the time axis using the relaxation time $\omega^2_{\ell,m}/\gamma$. The intrinsic friction was disregarded in our calculations since it was 3 orders of magnitude smaller than the Brownian friction.

In Supplemental Material Fig. 9 [77] Eq. (A30) was used to fit the intrinsic friction as a function of the mode frequencies for $\Phi = 0.037$. Since higher values of $\Phi \geqslant 0.15$ generate a Young's modulus Eq. (A30) is no longer valid. Based on the calculations presented in Appendix A 6, we can calculate the frequency of the vesicles as

$$\omega_{\ell,m}(\Phi)^2 = \frac{4\pi}{Mr_0^2}\bigg[\kappa(\ell+2)(\ell+1)\ell(\ell-1) + Y_{2\text{D}}(\Phi)\left(\frac{3(\ell^2+\ell-2)}{3(\ell^2+\ell)-2}\right)\bigg], \tag{46}$$

where the definition of $Y_{2\text{D}}(\Phi)$ is in Eq. (45).

2. Dynamics of larger shape transformations

The movies **SM_AVh_GKB_L_nu0.6**, **SM_RBC_c0**, and **SM_RBC_c0.006** illustrate the evolution from oblate initial states to the shapes shown in Figs. 7 and 8, respectively, for vesicles with a reduced volume $\nu \ll 1$ and a red blood cell model. We close by exploring the timescale on which these transformations occur in a vacuum when the vesicles are simulated using mesh dynamics.

In Fig. 11, we plotted the temporal evolution of the bending energy as a proxy for the evolution of the shape transformations for vesicles with reduced volumes $\nu \leqslant 1$. For $\nu = 1$, the initial bending energy of $E_b = 8\pi\kappa = 502.6 k_B T$ about doubles when each of the $N = 1002$ surface modes absorbs the thermal energy of $k_B T/2$. For smaller ν, this increase is more than compensated by the decrease of the bending energy for the initial oblate or prolate ellipsoid to the shapes illustrated in Fig. 7. We have rescaled the time axis in Fig. 11 with the time, $\tau_{2,m}$, it takes to complete the slowest surface oscillations in equilibrium. As is clear from the data, the shape transformation occurs in all cases extremely rapidly on a fraction of this time and without the larger and larger spatial distances over which the vertices need to move in the more strongly deflated vesicles in the least slowing down the process. We conclude that in mesh dynamics simulations, where the bilayer is coupled to an explicit solvent or hydrodynamic solver, the vesicle dynamics would be completely dominated by the induced motion of the fluid.

H. Computational efficiency

Vesicle simulations using mesh dynamics for a continuum model are obviously “fast” compared to models with molecular resolution. But we also believe them to be quite useful within their own class for reasons inherent in the method as well as for unlocking the computational power of modern molecular dynamics codes.

1. Sampling efficiency

Regarding sampling, the computational effort is proportional to the ratio of the longest relaxation time in the system and the time step. In the case of underdamped mesh dynamics simulations,

$$\frac{\tau_{2,m}}{\sqrt{\Phi}\tau_{\ell_{\max},m}} \propto \frac{N}{\sqrt{\Phi}}, \tag{47}$$

while for overdamped mesh dynamics simulations with a damping constant $\gamma = (\sqrt{\Phi}\tau_{\ell_{\max},m})^{-1}$ of the order of the inverse time step this increases to

$$\frac{\gamma\tau_{2,m}^2}{\sqrt{\Phi}\tau_{\ell_{\max},m}} = \frac{\tau_{2,m}^2}{\left(\sqrt{\Phi}\tau_{\ell_{\max},m}\right)^2} \propto \frac{N^2}{\Phi}. \tag{48}$$

2. Algorithmic complexity

The second proportionality factor is the time required to complete all the calculations necessary to execute a single time step. For the calculation of the bending energies and forces, this timescales linearly with the number of vertices, N. However, our global area and volume potentials imply that for these parts of the calculation, the computational effort per time step increases as the second power of the number of vertices.

3. The efficiency of modern MD codes

Being compatible with standard molecular dynamics has the advantage that mesh dynamics can benefit from the enormous work done in this field to adapt codes to modern computer architectures. For example, we could run all vesicle simulations on GPUs without extra work because our mesh dynamics implementation in VCM is based on OpenMM.

TABLE II. The hardware specification of the GPUs used for the simulations.

GPU	Cores	Freq. (base)	Memory	Power	Price
1	3000	1.6 GHz	8 GB	250 W	∼\$700
2	16 000	2.2 GHz	24 GB	450 W	∼\$2000

We have benchmarked mesh dynamics on two GPUs installed on similar machines with different technical specifications (see Table II).

Our vesicle simulations are extremely light on memory (<250 MB) since the vesicle is represented by just $\sim 10^3$ vertices. The results for the runtime of a vesicle with N vertices simulated for $10\tau_{2,0}$ with $1\tau_{2,0}$ sampling rate (interrupt MD 10 times to retrieve simulation trajectories, velocities, etc.), were reported in Table III.

To appreciate these numbers, we recall that the above simulation times correspond to the generation of one statistically independent sample in equilibrium or to the time necessary to effect the larger shape transformations. We conclude that taking advantage of OpenMM’s parallelization, mesh dynamics simulations via VCM provide a fast and low-cost method for exploring vesicle shapes.

Furthermore, the above numbers reveal that for $N = 4002$ particles, the many-body interactions about double the execution time relative to the optimal N^2 scaling. In the present implementation, mesh dynamics thus risks losing its efficiency for larger system sizes or resolutions than we have considered.

V. DISCUSSION

A. Soft meshes versus hard meshes

Homogenous triangulations (top row in Fig. 1) represent the geometrical properties of surfaces more accurately than triangulations with identical numbers of vertices, but triangles of variable areas and shapes (bottom row in Fig. 1). Not surprisingly, most numerical studies of continuum models of fluid bilayer membranes employ “hard” meshes imposing this homogeneity. However, for evolving surfaces hard meshes need dynamic remeshing to relax deformation-generated stress and shear.

Here we propose to trade precision for flexibility and to use “soft” meshes, which can adapt to a large variety of shapes (Figs. 7 and 8) without generating a significant elastic restoring force toward the shape, for which their connectivity was optimized.

TABLE III. The energy consumption and runtime of the simulation samples for different hardware.

	GPU 1		GPU 2	
N	Runtime	Consumption	Runtime	Consumption
252	12 s	8.3×10^{-4} kWh	10 s	1.25×10^{-3} kWh
1002	3.83 min	1.6×10^{-2} kWh	3.66 min	2.75×10^{-2} kWh
4002	110 min	0.46 kWh	72 min	0.54 kWh

B. Robust curvature energy discretization

For hard meshes, there is little to choose between Gompper's and Kroll's [84] popular adaptation of Itzykson's [65] discretization of the curvature energy and the alternative formulation by Jülicher [66] (Supplemental Material Fig. 6 [77]). Remarkably, the Gompper and Kroll formula is almost as precise for soft fluctuating meshes as for homogeneous tilings. In contrast, there are appreciable discretization errors for Jülicher's formula, even though there seem to be smaller or no differences for the derived forces (Fig. 4). As we show in Supplemental Material Sec. IV [77], the reason for the higher precision of Itzykson's [65] discretization is the choice of the Voronoi instead of the Barycentric area for the normalization of the contribution of a plaquette (Fig. 14). Itzykson's and Jülicher's expressions for the numerator measuring the local curvature yield identical results.

However, the less precise formulations using the Barycentric area offer *vastly superior* numerical *robustness* for the evaluation of the curvature energy of soft meshes. Problems arise on triangulated meshes whenever a vertex moves out of the area defined by the vertices it is connected to (Fig. 17). While simple auxiliary potentials on the height of the triangles are sufficient to stabilize simulations using Barycentric area (Fig. 18), violations of the tiling conditions almost inevitably lead to irrecoverable errors for Voronoi-based formulas.

C. Mesh dynamics simulations

Mesh dynamics is formulated as a molecular dynamics compatible framework for the simulation of continuum models of fluid bilayer membranes, where the degrees of freedom are the vertices of two-dimensional meshes with fixed connectivity. In particular, we exploit the robustness of barycentric formulations of the curvature energy to employ *soft* meshes for which the in-plane motion of the vertices is only weakly constrained and which can adapt to a large variety of shapes. Furthermore, we found ways to implement the potentials controlling the *total* surface area and enclosed volume [80] as many-body potentials (Supplemental Material Eqs. (1) and (2) [77]). In contrast to single vertex Monte Carlo moves for the same model, solving the equations of motion for the coupled mesh degrees of freedom generates collective "moves" which globally redistribute the surface area and the enclosed volume.

The present first tests suggest that mesh dynamics is numerically efficient and can, for soft meshes, quantitatively reproduce characteristic large-scale behavior of fluid bilayer membranes without remeshing. Moreover, the dissipation free dynamics ensure that the vesicle dynamics will be dominated by the enclosed and surrounding fluid once the mesh is coupled to an explicit solvent or hydrodynamic solver.

D. A unified view of dynamic triangulation and mesh dynamics

Mesh dynamics shows that the surface dynamics can be largely decoupled from changes in mesh connectivity. In Sec. II C 3, we defined ensemble averages over the possible vesicles shapes, Eq. (7), as ensemble averages over the possible connectivities and vertex positions for the meshes representing the surfaces, Eq. (11). In particular, we argued that for soft meshes, it might be enough to integrate out the vertex positions for a fixed connectivity graph, $\mathcal{G}$, which is reasonably well adapted to the dominant shapes $\mathcal{S}$ in the ensemble, Eq. (14). Figure 7 illustrates that for sufficiently soft meshes, even shapes for reduced volumes $\nu \ll 1$ can be reliably simulated with a spherical mesh.

Obviously, there is no reason to make a dogma out of using fixed mesh connectivity. Dynamic triangulation [69,97] is the obvious solution to the limited shape transformations in pure mesh dynamics simulations for harder meshes (Fig. 7). As shown in Supplemental Material Fig. 8 [77], the appearance of notable deviations coincides with measurable increases in the average value of the auxiliary potential, $\langle U_h \rangle$ controlling the softness of our meshes. We have not yet tried to combine the two approaches, but since our description is based on a Hamiltonian, we see no principal obstacle to alternating between mesh dynamics simulations and connectivity-altering Monte Carlo moves to sample averages over the annealed ensemble of mesh connectivities. While mesh dynamics simulations would assure efficient nonlocal mass transport and surface dynamics, the regular dynamic retriangulation would keep the energy stored in the auxiliary potentials independent of the vesicle shape and hence prevent the corresponding effective elasticity from distorting the observed conformations. Obviously, the harder the mesh, the more frequently these moves need to be applied and the more often one needs to step out of the MD simulations.

VI. SUMMARY AND CONCLUSION

Most current simulations of continuum models of fluid bilayer membranes follow Gompper and Kroll [84] in using dynamic triangulation Monte Carlo schemes [68,69] together with a discretization of the curvature energy going back to Itzykson [65]. Here we have shown that an alternative formulation by Jülicher [66] offers vastly superior numerical robustness for the evaluation of the curvature energy on triangulated meshes with fluctuating triangle shapes and sizes. Curiously, the ultimate reason for the versatility of Jülicher's formulation lies in a comparatively mundane part of his expression: the choice of the Barycentric area for the normalization of the contribution of a plaquette (Fig. 14). It is the use of the Voronoi area for the same purpose in Itzykson's expression, which proves to be its undoing for irregular meshes.

Soft meshes can represent a large variety of shapes without requiring remeshing and are thus ideal for simulations of dynamically evolving surfaces. Here we have exploited the robustness of barycentric formulations of the curvature energy to propose mesh dynamics simulations of soft meshes as an alternative to dynamic triangulation for hard meshes. Mesh dynamics allows the simulation of continuum models of fluid bilayer membranes in a molecular dynamics framework, where the degrees of freedom are the vertices of a soft two-dimensional mesh with fixed connectivity whose in-plane motion is only weakly constrained. In particular, mesh dynamics simulation treats the conservation of the membrane area globally and not locally. There was no coupling between the unresolved in-plane flow of lipids and the in-plane motion of the vertices of our soft mesh: the bilayer area was dynamically redistributed over the entire mesh.

We have implemented mesh dynamics into the OpenMM molecular dynamics engine [32] via the virtual cell model [56] software package, allowing us to benefit from OpenMM's built-in ability to distribute calculations on GPUs and to automatically derive the forces corresponding to (multiparticle) potentials [32]. In the first step, we have established the numerical foundations of mesh dynamics. In particular, we (i) have introduced suitable auxiliary potentials for controlling the soft mesh representing the bilayer, (ii) have analyzed the time step of mesh dynamics simulations, and (iii) have shown them to be long-time stable. In the second step, we have focused on the physical validation and interpretation of the results of mesh dynamics simulations for vesicles represented by $N \sim 1000$ vertices with a typical radius of $1\ \mu m$ and fluid bilayer membranes with bending rigidities of $20 k_B T$.

As a first quantitative test of the method, we have analyzed surface modes for nearly spherical vesicles. While there are well-known theoretical predictions for their mean-square excitation [45,63], we have additionally derived the expected functional form of their autocorrelation functions for the Newtonian, Langevin, and Brownian vertex dynamics readily available in molecular dynamics engines.

With respect to the mean-square amplitudes of the surface modes, we demonstrated the ability of our method to generate the characteristic] signature $\langle |u_{\ell,m}|^2 \rangle \propto \frac{1}{\ell^4}$ of the long-wavelength bending modes of vesicles with fluid membranes and to quantitatively reproduce their theoretically expected amplitudes, Eq. (A17). Furthermore, our analysis revealed that the fixed mesh connectivity and the mesh dynamics auxiliary potential U_h combine to produce a small effective Young's modulus, $Y_{2D}(\Phi)$, which can be easily controlled via the softness Φ of the employed mesh.

The dynamical analysis showed that the relaxation of the surface modes for Newtonian, Langevin, and Brownian vertex dynamics could be quantitatively understood in a generalized Langevin framework with an intrinsic, mode number-dependent friction for the different surface modes. Importantly, the model's internal friction is negligible since even the longest wavelength surface modes remain underdamped in molecular dynamics simulations solving Newton's equations of motion for the vertices of our soft meshes. This feature is essential for the possibility of generating realistic vesicle dynamics in future simulations, where the present membrane model is coupled to hydrodynamic solvers or explicit (coarse-grain) solvent models since the surface mode dynamics of vesicles in nature are highly damped and dominated by the hydrodynamics of the surrounding and enclosed fluids [44,45].

First results of mesh dynamics simulations for the exploration of vesicle shapes with reduced volumes $\nu \ll 1$ and the behavior of (red blood) cells with composite membranes further demonstrated the utility of soft meshes and their ability to adapt to a large variety of vesicle shapes. In particular, the larger shape transformations occurred in our mesh dynamics simulations on the characteristic timescale of the slowest surface modes and can be simulated in a matter of minutes on standard GPUs.

Two limitations of the present work merit emphasis:

(i) When the area constraint is applied globally and not locally [88], a vertex represents a variable amount of bilayer corresponding to the instantaneous area of the associated plaquette. Interestingly, the general mesh Hamiltonian (16) generates an effective interaction, Eq. (20), homogenizing the plaquette areas. However, the corresponding equations of motion (22) are nontrivial to solve and require further study. This might be interesting in itself and necessary for the application of mesh dynamics to systems like soap bubbles, where inertial effects are important and sensitive to the mass distribution on the triangulated surface. Here we have studied mesh dynamics in the constant vertex mass approximation, where vertices follow standard Newtonian dynamics. We believe this approximation to be uncritical for lipid bilayer vesicles in aqueous solutions, where inertial effects are irrelevant. However, we have not yet demonstrated this in practice by coupling our vesicles to an explicit solvent or hydrodynamic solvers [55].

(ii) In general, continuum models require dynamic meshing techniques to explore the multitude of shapes that two-dimensional liquids can adopt in three dimensions. Mesh dynamics should thus, in general, be viewed as a *complement* to dynamic triangulation rather than a *substitute*. Since our description is based on a Hamiltonian, we see no principal obstacle to decoupling the surface dynamics from the remeshing by alternating between mesh dynamics simulations and connectivity-altering Monte Carlo moves. In particular, this combination should allow the simulation of surfaces with meshes of arbitrary Φ if the frequency of dynamic triangulation attempts is adjusted to the stiffness of the mesh. But again, we have not yet combined the two approaches in practice.

ACKNOWLEDGMENTS

We gratefully acknowledge the support of the Centre Blaise Pascal's IT test platform at ENS de Lyon (Lyon, France) for GPU and CPU facilities. The platform operates the SIDUS solution [98] developed by Dr. Emmanuel Quemener. M.R.E. acknowledges support from the Abdus-Salam ICTP through the Associates Programme (2019–2025). Furthermore, we acknowledge our referees for their rigorous and constructive comments.

APPENDIX A: FLUCTUATION ANALYSIS FOR NEARLY SPHERICAL VESICLES

The ground-state shape of a vesicle is a function of its material and geometrical properties. However, due to thermal fluctuations, random undulations appear on the surface. The shapes of nearly spherical vesicles can be described as a sum of normal modes [84]. Various properties of the membrane, such as its energy or dynamics, can be understood by studying these modes. Undulation at each point, $r(\theta, \phi)$, can be written as a radial displacement relative to the average radius, r_0,

$$r(\theta, \phi) = r_0[1 + g(\theta, \phi)]. \tag{A1}$$

Because the membrane is nearly spherical, it is convenient to expand $g(\theta, \phi)$ in terms of the spherical harmonics, $Y_{\ell,m}(\theta, \phi)$,

$$g(\theta, \phi) = \sum_{\ell=0}^{\ell_{\max}} \sum_{m=-\ell}^{\ell} u_{\ell,m} Y_{\ell,m}(\theta, \phi). \tag{A2}$$

$u_{\ell,m}$, is the normal mode amplitude, and we have used the definition of the normalized spherical harmonics,

$$Y_{\ell,m}(\theta,\phi)=\sqrt{\frac{2\ell+1}{4\pi}}\sqrt{\frac{(\ell-|m|)!}{(\ell+|m|)!}}\,P_\ell^m(\cos\theta)\,e^{im\phi},\qquad\text{(A3)}$$

that is a function of the associated Legendre polynomials, $P_\ell^m(x)$.

Following the same logic, surface undulation mode amplitudes for a closed surface can be calculated using the following surface integral:

$$\langle|u_{\ell,m}|^2\rangle=\int d\Omega\,Y^*_{\ell,m}(\theta,\phi)\left(\frac{r(\theta,\phi)-r_0}{r_0}\right).\qquad\text{(A4)}$$

1. The area of a fluctuating spherical shape

The area of a membrane patch, $dA=r^2d\Omega$, in terms of spherical harmonics (up to second order in g) is [34]

$$dA=r_0^2\left(1+g^2+\tfrac{1}{2}g\mathcal{L}^2g\right)d\Omega,\qquad\text{(A5)}$$

where the angular momentum operator $\mathcal{L}^2$ has the standard definition,

$$\mathcal{L}^2=-\frac{1}{\sin\theta}\frac{\partial}{\partial\theta}\left(\sin\theta\frac{\partial}{\partial\theta}\right)-\frac{1}{\sin^2\theta}\frac{\partial^2}{\partial\phi^2}.\qquad\text{(A6)}$$

Taking the integral yields the area of a fluctuating surface A,

$$\begin{aligned}A&=\int dA=r_0^2\int\left(1+g^2+\frac{1}{2}g\mathcal{L}^2g\right)d\Omega\\&=r_0^2\left\{4\pi+\sum_\ell|u_{\ell,m}|^2\left[1+\frac{1}{2}\ell(\ell+1)\right]\right\}.\end{aligned}\qquad\text{(A7)}$$

Compared to a sphere, a larger area is needed to accommodate fluctuations. The excess area energy cost can be calculated by substituting the derived expression in Eq. (1),

$$\begin{aligned}E_A&=\frac{1}{2}k_A\frac{\left(A-4\pi r_0^2\right)^2}{4\pi r_0^2}\\&=\frac{1}{8\pi}k_Ar_0^2\left\{\sum|u_{\ell,m}|^2\left[1+\frac{1}{2}\ell(\ell+1)\right]\right\}^2.\end{aligned}\qquad\text{(A8)}$$

2. The volume of a fluctuating spherical shape

The volume enclosed by a fluctuating membrane can be calculated by integrating over the volume element enclosed by the membrane, dV. Keeping terms up to the second order in g,

$$\begin{aligned}V&=\int dV=\frac{1}{3}\int r\,dA\\&=\frac{1}{3}\int r^3d\Omega=\frac{1}{3}r_0^3\int(1+g)^3d\Omega\\&=\frac{1}{3}4\pi r_0^3+r_0^3\sum_\ell|u_{\ell,m}|^2.\end{aligned}\qquad\text{(A9)}$$

Similar to Sec. A 1, we can use Eq. (2) to calculate the energy due to volume fluctuations,

$$E_V=\frac{1}{2}k_V\frac{\left(V-\frac{4}{3}\pi r_0^3\right)^2}{\frac{4}{3}\pi r_0^3}=\frac{3}{8\pi}k_Vr_0^3\left(\sum|u_{\ell,m}|^2\right)^2.\qquad\text{(A10)}$$

The reduced volume of a shape, ν, is the ratio of its volume to the ratio of the volume of a sphere with the same surface area,

$$\nu=6\sqrt{\pi}VA^{-\frac{3}{2}}.\qquad\text{(A11)}$$

A perfect sphere has a reduced volume of $\nu=1$. To accommodate fluctuations on the surface, a shape with a reduced volume, $\nu<1$, is required [99]. Equations (A7) and (A9) can be used to calculate the reduced volume required by a surface fluctuating with a set of mode amplitudes,

$$\begin{aligned}\nu&=\frac{1+\frac{3}{4\pi}\sum|u_{\ell,m}|^2}{\left\{1+\frac{1}{4\pi}\sum|u_{\ell,m}|^2\left[1+\frac{1}{2}\ell(\ell+1)\right]\right\}^{3/2}}\\&\approx1-\frac{3}{8\pi}\sum|u_{\ell,m}|^2[\ell(\ell+1)-1].\end{aligned}\qquad\text{(A12)}$$

3. Bending fluctuations

The energy of a membrane dominated by bending and without area or volume constraints can be described by Eq. (4). If we assume that the spontaneous radius is the same everywhere on the membrane surface, then the curvature energy of the membrane with spontaneous radius, r_s, is [34]

$$E_b=\frac{1}{2}\kappa\int dA\left(\nabla\cdot\vec{n}-\frac{2}{r_s}\right)^2.\qquad\text{(A13)}$$

The surface normal, $\vec{n}$, is defined as a function of the equation of the surface, $R(r)=r-r_0[1+g(\theta,\phi)]=0$,

$$\vec{n}=\frac{\vec{\nabla}R(r)}{|\vec{\nabla}R(r)|},\qquad\text{(A14)}$$

where (r,θ,ϕ) are the spherical coordinates. Expanding Eq. (A13) in terms of spherical harmonics [45],

$$\begin{aligned}E^b_{\ell,m}=&\,8\pi\kappa+\frac{1}{2}\kappa\sum_{\ell>1}|u_{\ell,m}|^2(\ell+2)(\ell-1)\\&\times[\ell(\ell+1)-4\alpha+2\alpha^2],\end{aligned}\qquad\text{(A15)}$$

and applying the equipartition theory, we may estimate the fluctuation amplitudes [34,44] of a bending dominant membrane without constraints as

$$\langle|u_{\ell,m}|^2\rangle=\frac{k_BT}{\kappa}\frac{1}{(\ell+2)(\ell-1).[\ell(\ell+1)-4\alpha+2\alpha^2]}\qquad\text{(A16)}$$

$\alpha=r_0/r_s$ is the ratio of the radius of the membrane and the spontaneous radius. Since the contributions from the area and volume energies are of the order, $\mathcal{O}(u^4_{\ell,m})$, we have not included them in the derivation of Eq. (A16). For a vesicle with $\alpha=0$, the amplitudes simplify to

$$\langle|u_{\ell,m}|^2\rangle=\frac{k_BT}{\kappa}\frac{1}{(\ell+2)(\ell+1)\ell(\ell-1)}.\qquad\text{(A17)}$$

Notice that the amplitude of each mode is only a function of the mode number, ℓ, and temperature to bending rigidity ratio, k_BT/κ, and (as expected) independent of the radius (size) of the system.

4. Spherical shell fluctuations

Composite membranes like the nuclear envelope or the red blood cell also include components made of polymers that have elastic properties. The surface mode fluctuations of these systems can be described in terms of their two-dimensional Young's modulus, Y_{2D}, and the pressure difference, Δp, between the surrounding and enclosed fluid [63],

$$\begin{aligned} k_BT\langle|u_{\ell,m}|^2\rangle^{-1} = {}& \kappa(\ell+2)(\ell+1)\ell(\ell-1) \\ & - \Delta p\, r_0^3\left[1+\frac{1}{2}\ell(\ell+1)\right] \\ & + Y_{2D}\, r_0^2\left[\frac{3(\ell^2+\ell-2)}{3(\ell^2+\ell)-2}\right]. \end{aligned} \tag{A18}$$

For such systems, the surface fluctuation amplitudes are no longer size independent. This corresponds to a buckling transition from a bending dominant spherical shape to a faceted one determined by the dimensionless Föppl-von Kármán number $\Gamma = Y_{2\mathrm{D}} r_0^2/\kappa$ [89].

5. Normal force on the vesicle surface

Following Ref. [45], the curvature of a surface with $C_0 = 0$ is defined as

$$H = C_1 + C_2 = \vec{\nabla}\cdot\vec{n} = \frac{2}{r}\left(1+\frac{r_0}{2r}\mathcal{L}^2 g\right); \tag{A19}$$

for small g we can approximate $1/r$ with $\frac{1}{r_0}(1-g)$. The force density on the surface of the vesicle is defined as $-\kappa\nabla^2 H$. Taking the Laplacian of the above equation,

$$\nabla^2 H = \left[\frac{1}{r^2}\frac{\partial}{\partial r}\left(r^2\frac{\partial}{\partial r}\right) - \frac{1}{r^2}\mathcal{L}^2\right]\left[\frac{2}{r}\left(1+\frac{r_0}{2r}\mathcal{L}^2 g\right)\right]. \tag{A20}$$

The radial derivative calculations are as follows:

$$\begin{aligned} & \frac{1}{r^2}\frac{\partial}{\partial r}\left\{r^2\frac{\partial}{\partial r}\left[\frac{2}{r}\left(1+\frac{r_0}{2r}\mathcal{L}^2 g\right)\right]\right\} \\ & = \frac{-2}{r^2}\frac{\partial}{\partial r}\left(1+\frac{r_0}{r}\mathcal{L}^2 g\right) \\ & = \frac{2r_0}{r^4}\mathcal{L}^2 g. \end{aligned} \tag{A21}$$

Carrying out the angular derivative, we get

$$-\frac{1}{r^2}\mathcal{L}^2\left[\frac{2}{r}\left(1+\frac{r_0}{2r}\mathcal{L}^2 g\right)\right] = -\frac{r_0}{r^4}\mathcal{L}^2(\mathcal{L}^2 g). \tag{A22}$$

Therefore, we arrive at the following expression for Eq. (A20):

$$\nabla^2 H = \frac{r_0}{r^4}[2\mathcal{L}^2 g - \mathcal{L}^2(\mathcal{L}^2 g)]. \tag{A23}$$

The normal force angular density can be calculated as a function of θ, ϕ,

$$\begin{aligned} F(\theta,\phi) &= -\int \kappa\nabla^2 H\frac{dA}{d\Omega} \\ &= \kappa\frac{r_0}{r^4}[2\mathcal{L}^2 g - \mathcal{L}^2(\mathcal{L}^2 g)]r^2\left(1+\frac{r_0^2}{2r^2}g\mathcal{L}^2 g\right) \\ &= \frac{\kappa r_0}{r^2}[2\mathcal{L}^2 g - \mathcal{L}^2(\mathcal{L}^2 g)] + \mathcal{O}(g^3). \end{aligned} \tag{A24}$$

Taking the spherical Fourier transform of the above equation yields the force on each mode,

$$\begin{aligned} f_{\ell,m} &= \int F(\theta,\phi)Y^*_{\ell,m}(\theta,\phi)d\Omega, \\ f_{\ell,m} &= -\frac{\kappa}{r_0}u_{\ell,m}(\ell+2)(\ell+1)\ell(\ell-1). \end{aligned} \tag{A25}$$

6. Dynamics and timescale calculations

We can write Newton's equation to describe the motion of points on a spherical vesicle oscillating in a vacuum as a function of the angular coordinates θ with a radius r_0 and a homogeneous density $M/4\pi r_0^2$,

$$\begin{aligned} \frac{M}{4\pi r_0^2}\frac{dA}{d\Omega}\ddot{r}(\theta,\phi,t) &= F(\theta,\phi), \\ \frac{Mr_0}{4\pi}\sum_{\ell,m}\ddot{u}_{\ell,m,t}Y_{\ell,m}(\theta,\phi) &= F(\theta,\phi), \end{aligned} \tag{A26}$$

where $F(\theta,\phi)$ is the force on the vesicle at a specific spherical coordinate. We can derive an expression for the dynamics of the vesicle modes by taking the spherical Fourier transform of the above equation. The Fourier transform of the left-hand side is

$$\begin{aligned} & \frac{Mr_0}{4\pi}\int d\Omega Y^*_{\ell,m}(\Omega)\sum_{\ell',m'}\ddot{u}_{\ell',m'}(\Omega,t)Y_{\ell',m'}(\Omega) \\ & = \frac{Mr_0}{4\pi}\ddot{u}_{\ell,m}(t). \end{aligned} \tag{A27}$$

We can use Eq. (A17) to derive the normal force of each mode,

$$\begin{aligned} f_{\ell,m}(t) &= -\frac{1}{r_0}\frac{\partial}{\partial u_{\ell,m}}E_b \\ &= -\frac{\kappa}{r_0}u_{\ell,m}(t)(\ell+2)(\ell+1)\ell(\ell-1), \end{aligned} \tag{A28}$$

in agreement with Eq. (A25). Alternatively, in the case where the spontaneous curvature of the vesicle is zero ($C_0 = 0$), the normal force surface density on the vesicle is $F = -\kappa\nabla^2(C_1 + C_2)$ [44]. Therefore, the normal force angular density can be calculated with $F(\theta,\phi) = F \times (dA/d\Omega)$. A more sophisticated force expression can also be derived for a nonzero spontaneous curvature, as demonstrated by Ref. [45].

Putting Eqs. (A27) and (A28) together, we draw an expression for the mode dynamics,

$$\begin{aligned} \ddot{u}_{\ell,m} &= -\frac{4\pi\kappa}{Mr_0^2}u_{\ell,m}(t)(\ell+2)(\ell+1)\ell(\ell-1), \\ \ddot{u}_{\ell,m} &= -\omega^2_{\ell,m}u_{\ell,m}, \end{aligned} \tag{A29}$$

where the oscillation angular frequency of each mode, $\omega_{\ell,m}$ is defined as

$$\omega_{\ell,m} = \sqrt{\frac{4\pi\kappa}{Mr_0^2}(\ell+2)(\ell+1)\ell(\ell-1)}. \tag{A30}$$

Since the period of oscillation, $\tau_{\ell,m} = 2\pi/\omega_{\ell,m}$, is proportional to the inverse of $\omega_{\ell,m}$, the smallest mode number ($\ell = 2$) corresponds to the slowest shape change dynamics.

The Langevin equation can be used to describe the dynamics of a vesicle under constant friction ζ in contact with a heat bath at temperature T,

$$\begin{aligned} m\ddot{x} + \zeta\dot{x} + kx &= F_\eta, \\ F_\eta &= \sqrt{2k_BT\zeta}\,\eta(t), \end{aligned} \tag{A31}$$

where $\eta(t)$ is the time derivative of a Wiener process with the following properties,

$$\begin{aligned} \langle\eta(t)\rangle &= 0, \\ \langle\eta(t)\eta(t')\rangle &= \delta(t-t'). \end{aligned} \tag{A32}$$

Following a similar procedure, the mode amplitudes for Langevin dynamics can be derived,

$$\begin{aligned} \frac{Mr_0}{4\pi}\ddot{u}_{\ell,m} + \frac{\zeta r_0}{4\pi}\dot{u}_{\ell,m} + \frac{Mr_0}{4\pi}\omega_{\ell,m}^2 u_{\ell,m} &= F_\eta, \\ \ddot{u}_{\ell,m} + \gamma\dot{u}_{\ell,m} + \frac{k_{\ell,m}}{M}u_{\ell,m} &= \frac{4\pi}{Mr_0}F_\eta, \end{aligned} \tag{A33}$$

where $k_{\ell,m} = M\omega_{\ell,m}^2$ and we have substituted $\zeta = \gamma M$. Equation (A33) describes a damped oscillation with frequency $\omega'_{\ell,m} = \sqrt{\omega_{\ell,m}^2 - \gamma^2/4}$. The nature of damping depends on $\omega'_{\ell,m}$. Real positive values of $\omega'_{\ell,m}$ describe an underdamped system, $\omega'_{\ell,m} = 0$ a critically damped, and if $\omega'_{\ell,m}$ is complex, then the system is overdamped. We can use Eq. (A30) to calculate the characteristic critical mode number, ℓ_{crit}, as a function of the friction,

$$\ell_{\text{crit}} \approx \frac{1}{2}\left(\frac{Mr_0^2}{\pi\kappa}\right)^{\frac{1}{4}}\sqrt{\gamma}. \tag{A34}$$

For a given γ, mode numbers larger than the critical mode (shorter wavelengths), $\ell > \ell_{\text{crit}}$ are underdamped, and longer wavelengths are overdamped.

The autocorrelation of the mode amplitudes for an underdamped vesicle is

$$\begin{aligned} &\langle u_{\ell,m}(t)u_{\ell,m}(0)\rangle \\ &\quad = \langle|u_{\ell,m}|^2\rangle e^{-\frac{\gamma}{2}t}\left[\cos(\omega'_{\ell,m}t) + \frac{\gamma}{2\omega'_{\ell,m}}\sin(\omega'_{\ell,m}t)\right]. \end{aligned} \tag{A35}$$

In the equation above, the relaxation time of the system is $1/\gamma$. The mode amplitude autocorrelation for a critically damped vesicle is

$$\langle u_{\ell,m}(t)u_{\ell,m}(0)\rangle = \langle|u_{\ell,m}|^2\rangle e^{-\frac{\gamma}{2}t}\left(1 + \frac{\gamma}{2}t\right). \tag{A36}$$

Finally, the mode amplitude autocorrelation for an overdamped vesicle is

$$\begin{aligned} &\langle u_{\ell,m}(t)u_{\ell,m}(0)\rangle \\ &\quad = \langle|u_{\ell,m}|^2\rangle e^{-\frac{\gamma}{2}t} \\ &\quad\quad \times\left[\sinh(|\omega'_{\ell,m}|t) + \frac{2}{\gamma}|\omega'_{\ell,m}|\cosh(|\omega'_{\ell,m}|t)\right]. \end{aligned} \tag{A37}$$

The vesicle motion for the high friction limit of Eq. (A31) where inertial forces can be disregarded, is captured by the Brownian equation,

$$\frac{r_0}{4\pi}\zeta\dot{u}_{\ell,m}(t) + \frac{r_0}{4\pi}k_{\ell,m}u_{\ell,m}(t) = F_\eta. \tag{A38}$$

The autocorrelation of the mode amplitudes takes the simple form

$$\langle u_{\ell,m}(t)u_{\ell,m}(0)\rangle = \langle|u_{\ell,m}|^2\rangle e^{-t/\tau_\zeta}. \tag{A39}$$

The relaxation time of the system, $\zeta/k_{\ell,m} = \gamma/\omega_{\ell,m}^2$, is calculated using the ratio of the harmonic force stiffness and the friction in the system.

The same procedure can be used to understand the behavior of modes when a vesicle fluctuates in a fluid environment. The bending force will have the same form since it depends only on the vesicle properties. However, the velocities of surface patches on the vesicle are dominated by the hydrodynamics of the surrounding and enclosed fluid. The autocorrelation of the surface mode amplitudes for such a system [45] can then be obtained by deriving the velocity field on the surface of the vesicle through the Stokes equation of motion [99].

APPENDIX B: TRIANGULATED SURFACES

1. Euler identity

Triangulated surfaces have interesting properties. A flat surface with a homogeneous distribution of vertices is tiled with isosceles triangles where each vertex is connected to exactly six neighbors (degree 6). However, this is not the case for curved surfaces. A closed surface comprises a mixture of vertices with different degrees. If only vertex degrees 5, 6, and 7 are present in a closed triangulated mesh, then the difference in the number of vertices with degrees 5 and 7 is a function of the genus, χ, of the surface [89],

$$N_5 - N_7 = 12(1-\chi). \tag{B1}$$

2. Area and volume

Since triangles on the meshes do not overlap, the total area of the surface can be calculated by summing over individual triangle areas. The area of each triangle can be easily calculated by taking half the magnitude of the cross product of two adjacent edges corresponding to the illustrated blue surface between $\overrightarrow{BA}$ and $\overrightarrow{CA}$ in Fig. 12:

$$A = \sum_{\text{tri}}\frac{1}{2}|\overrightarrow{BA}||\overrightarrow{CA}|\sin(\theta_{\text{BAC}}), \tag{B2}$$

$\sum_{\text{tri}}$, sums over all triangles on the mesh. The volume of a tetrahedron, v_i, with a surface triangle ABC as one of its faces and point, X, as its fourth vertex can be calculated using the triple product of the vectors in Fig. 12,

$$v_i = \tfrac{1}{6}\overrightarrow{AB}\times\overrightarrow{AC}\cdot\overrightarrow{AX}. \tag{B3}$$

The volume of tetrahedra can have negative signs depending on the coordinates of X. By always selecting vectors $\overrightarrow{AB}$ and $\overrightarrow{AC}$ such that their cross product points toward inside the mesh, the sum over, v_i, results in the mesh volume independent of the coordinate choice for X, even for the most

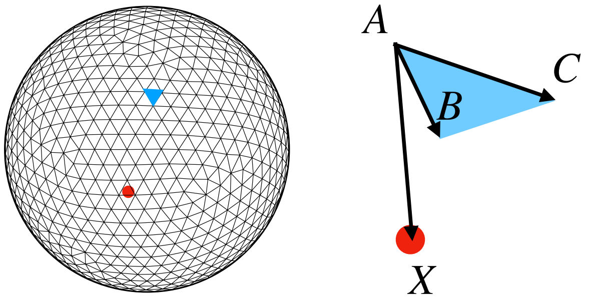

FIG. 12. Volume of a tetrahedron with a mesh triangle as one of its faces and an arbitrary point, X as its fourth vertex is calculated with the triple product of two vectors on the triangle and a third vector that points to X.

complicated shapes:

$$V = \sum_{tri} v_i. \tag{B4}$$

3. Approximate bending energies from dihedral angles

Kantor and Nelson [59] proposed approximating the energy described by Eq. (4) in terms of the dihedral angle between adjacent triangles,

$$E_b^{\text{Dihedral}} = k_b^{\text{Dihedral}} \sum_{<i,j>} (1 - \cos\phi_{ij}). \tag{B5}$$

In Eq. (B5) the sum runs over all edges (or triangle pairs) and ϕ_{ij} is the angle between triangle normals adjacent to edge ℓ_{ij} that connects vertex i and j [see Fig. 13(b)]. As discussed in detail by Gompper and Kroll [84], the relation between k_b^{Dihedral} in Eq. (B5) and κ in Eq. (4) is shape dependent (for a spherical shape $k_b^{\text{Dihedral}} \approx \frac{\sqrt{3}}{2}\kappa$) and therefore not appropriate for describing the curvature of nonspherical shapes. The triangle pair potential is simple but fails to calculate the curvature of saddle points correctly. Another problem with the triangle pair potential is that it is only a function of the dihedral angle, and subsequently, the shape and size of the surface triangles do not contribute to the surface curvature. This is a nice feature since the total bending curvature of a shape should be independent of the mesh size. But, it is not appropriate for surfaces tiled with a wide spread of triangle sizes that may result in a tiny triangle pair contributing the same to the bending curvature as a gigantic one with the same dihedral angle, ϕ_{ij}.

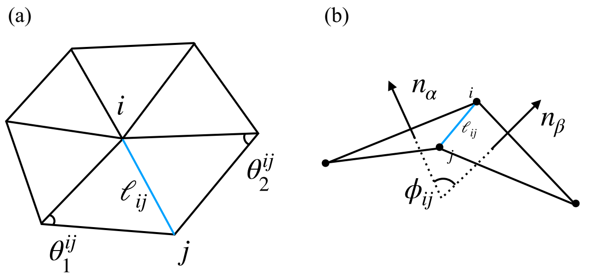

FIG. 13. (a) The angles θ_1^{ij} and θ_2^{ij} associated with the edge ℓ_{ij} are used to calculate the distance between vertices in a dual lattice [100]. (b) An arbitrary edge, ℓ_{ij}, on a triangulated surface sketched together with its adjacent triangles. The angle ϕ_{ij} is defined as the angle between normal triangular vectors, denoted by n_α and n_β.

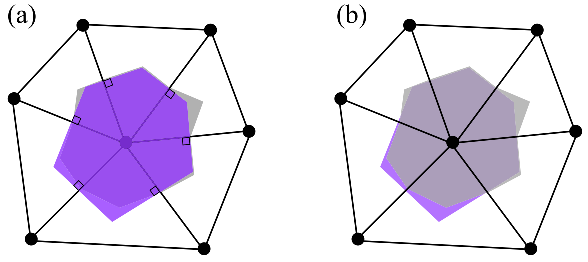

FIG. 14. (a) The Voronoi and (b) the Barycentric area of an arbitrary plaquette. The difference between the two vertex areas is emphasized by illustrating one area in the background and the other in the foreground.

The bending energy [Eq. (4)] can be discretized in terms of the mean curvature at each vertex $H_i = C_1 + C_2$, and the area associated with the vertex, a_i,

$$\begin{aligned} E_b &= \frac{1}{2}\kappa \int dA[C_1 + C_2 - C_0]^2 \\ &\equiv \frac{1}{2}\kappa \sum_i a_i[H_i - C_0]^2 \\ &= \frac{1}{2}\kappa \sum_i a_i\big[H_i^2 - 2H_iC_0 + C_0^2\big]. \end{aligned} \tag{B6}$$

4. The formulation by Itzykson, Gompper, and Kroll

In 1986, Itzykson calculated the Laplacian of a scalar field on a triangulated surface [65]. Since the mean curvature at each point, $\vec{r}$, on a surface patch with normal vector, $\vec{n}$, is defined as $H = \vec{n} \cdot \Delta\vec{R}$ (Δ is the Laplace–Beltrami operator), Gompper and Kroll used Itzykson's formulation to calculate the mean curvature of a vertex on a triangulated mesh [84] as

$$H_i^{\text{GK}} = \vec{n}_i \cdot \Delta\vec{r} \equiv \frac{1}{a_i^V}\vec{n} \cdot \left[\frac{\sum_{j(i)} \tilde{\ell}_{ij}}{\ell_{ij}}(\vec{r}_i - \vec{r}_j)\right]. \tag{B7}$$

The sum in $\sum_{j(i)}$ runs over all vertex neighbors of i. ℓ_{ij} is the length of the edge between vertex i and j, and $\vec{r}_i$ and $\vec{r}_j$ are the position vectors of the corresponding vertices. $\tilde{\ell}_{ij}$ is the length of a bond in the dual lattice and is defined as $\tilde{\ell}_{ij} = \frac{1}{2}\ell_{ij}(\cot\theta_1^{ij} + \cot\theta_2^{ij})$. The Voronoi area [Fig. 14(a)] associated with each vertex a_i^V, can be calculated using these two lengths,

$$a_i^V = \frac{1}{4}\sum_{j(i)} \tilde{\ell}_{ij}\ell_{ij}. \tag{B8}$$

The surface normal, $\vec{n}_i$, of a plaquette [assembly of triangles with a common vertex as sketched in Fig. 13(a)] is as follows [101]:

$$\vec{n}_i = \frac{\sum_{T(i)} \theta_T^i\, \vec{n}_T^i}{\left|\sum_{T(i)} \theta_T^i\, \vec{n}_T^i\right|}, \tag{B9}$$

where $\sum_{T(i)}$ runs over all triangles that include vertex i, θ_T^i and $\vec{n}_T^i$ are, respectively, the angle of a triangle at vertex,

i, and its surface normal vector. It should be noted that the Laplacian and the normal vector are in the same direction in three-dimensional space [84], which leads to the following definition for the surface bending energy,

$$E_b^{\rm GK} = \frac{1}{2}\kappa \sum_i \frac{1}{a_i^V}\left[\sum_{j(i)} \frac{\tilde{\ell}_{ji}}{\ell_{ij}}(\vec{r}_i - \vec{r}_j)\right]^2 - 2\frac{2}{r_s}\vec{n}_i \cdot \left[\sum_{j(i)}\frac{\tilde{\ell}_{ji}}{\ell_{ij}}(\vec{r}_i-\vec{r}_j)\right] + \frac{4}{r_s^2}a_i^V. \tag{B10}$$

Equation (B10) was derived for surfaces that have triangles with the same shape and size and are not obtuse [65]. As also discussed by Gompper and Kroll [84], Eq. (B10) can get unstable since the sign of $\tilde{\ell}_{ji}$ can become negative for obtuse triangles. By introducing restrictions on the length of mesh edges (and maximizing the probability of the appearance of acute triangles), Gompper and Kroll successfully modeled vesicles with an infinite spontaneous curvature radius ($C_0 = 0$) on dynamically triangulated surfaces.

5. Jülicher's formulation

Jülicher described the mean curvature of a lattice point by taking the average of the dihedral angles of neighboring triangles on a plaquette with the Barycentric area of the central vertex [66],

$$H_i^{\rm J} = \frac{1}{a_i^B}\sum_{j(i)}\frac{1}{2}\ell_{ij}\phi_{ij}. \tag{B11}$$

Here, ℓ_{ij} and ϕ_{ij} have the same definition as in Fig. 13(b). The area element associated with each vertex, a_i^B, is the Barycentric area [Fig. 14(b)] that is calculated as one third of the sum of the area of all triangles that have vertex i in common,

$$a_i^B = \frac{1}{3}\sum_{{\rm tri}(i)} a_{\rm tri}. \tag{B12}$$

Substituting in Eq. (B6) results in the total mean curvature energy of a mesh with spontaneous curvature defined as $C_0 = 2/r_s$ of a triangulated surface,

$$E_b^{\rm J} = \frac{1}{2}\kappa\sum_i\frac{1}{a_i^B}\left[\sum_{j(i)}\frac{1}{2}(\ell_{ij}\phi_{ij})\right]^2 - 2\frac{2}{r_s}\left[\sum_{j(i)}\frac{1}{2}(\ell_{ij}\phi_{ij})\right] + \frac{4}{r_s^2}a_i^B. \tag{B13}$$

We show in Supplemental Material Sec. IV [77] that for a given plaquette, the numerators in both Gompper and Kroll's [Eq. (B10)] and Jülicher's [Eq. (B13)] models calculate approximately the same value for small curvatures,

$$\left[\sum_{j(i)}\frac{1}{2}(\ell_{ij}\phi_{ij})\right]^2 \approx \left[\sum_{j(i)}\frac{\tilde{\ell}_{ij}}{\ell_{ij}}(\vec{r}_i-\vec{r}_j)\right]^2. \tag{B14}$$

Hence, the difference in the bending energy of a plaquette for these two models mainly originates from the weight (area) associated with each central vertex.

6. Alternative hybrid formulations

The difference in the associated vertex area in the bending energy models inspired us to use two new models to estimate the total curvature of plaquettes by swapping the weights. The Gompper&Kroll-Barycentric,

$$E_b^{\rm GKB} = \frac{1}{2}\kappa\sum_i\frac{1}{a_i^B}\left[\sum_{j(i)}\frac{\tilde{\ell}_{ij}}{\ell_{ij}}(\vec{r}_i-\vec{r}_j)\right]^2 - 2\frac{2}{r_s}\left[\sum_{j(i)}\frac{\tilde{\ell}_{ij}}{\ell_{ij}}(\vec{r}_i-\vec{r}_j)\right] + \frac{4}{r_s^2}a_i^B, \tag{B15}$$

and the Jülicher-Voronoi,

$$E_b^{\rm JV} = \frac{1}{2}\kappa\sum_i\frac{1}{a_i^V}\left[\sum_{j(i)}\frac{1}{2}(\ell_{ij}\phi_{ij})\right]^2 - 2\frac{2}{r_s}\left[\sum_{j(i)}\frac{1}{2}(\ell_{ij}\phi_{ij})\right] + \frac{4}{r_s^2}a_i^V. \tag{B16}$$

APPENDIX C: THE ENERGY LANDSCAPE SURROUNDING INDIVIDUAL VERTICES

To understand the effect of the physical and auxiliary potentials on the stability of mesh dynamics simulations, we have explored the $3d$ energy landscape for a *single* mobile vertex i in an otherwise frozen conformation of a spherical fluctuating random mesh,

$$\begin{aligned}\Delta U(\boldsymbol{q}_i') &= U(\mathcal{G},\{\boldsymbol{q}'\}) - U(\mathcal{G},\{\boldsymbol{q}\}),\\ \{\boldsymbol{q}\} &= \{\boldsymbol{q}_1,\boldsymbol{q}_2,,\ldots,\boldsymbol{q}_i,\ldots,\boldsymbol{q}_N\},\\ \{\boldsymbol{q}'\} &= \{\boldsymbol{q}_1,\boldsymbol{q}_2,,\ldots,\boldsymbol{q}_i',\ldots,\boldsymbol{q}_N\}.\end{aligned} \tag{C1}$$

It is obviously difficult to draw definite conclusions from a single, randomly chosen example, but we believe that the exercise nevertheless provides useful insights into the reason why it is difficult to run mesh dynamics simulations for soft meshes with Voronoi-based discretizations of the bending energy.

The chosen mesh is illustrated in Fig. 15 (left). All the reference coordinates $\{\boldsymbol{q}\}$ are located on the surface of a sphere

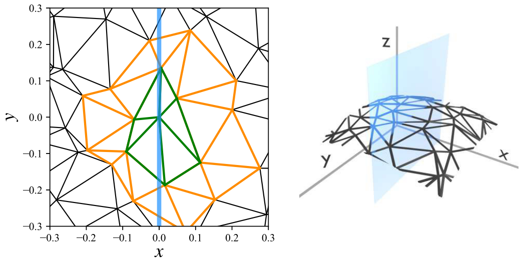

FIG. 15. Left: A 2D representation of a selected plaquette (left panel) on a fluctuating random mesh indicated with green bonds. The central vertex of the green plaquette is also a member of the neighbor plaquettes indicated with orange edges. Right: The two-dimensional cuts through the energy landscape are: (1) a curved surface on a sphere that goes through the mesh vertices (left column in Figs. 16–18) and (2) a straight surface (blue plane) perpendicular to the mesh surface (right column in Figs. 16–18).

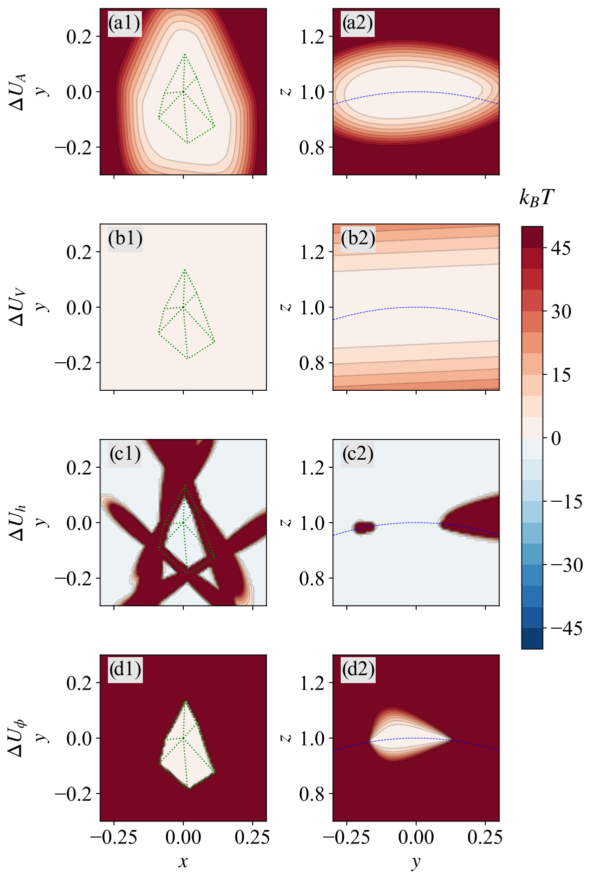

FIG. 16. The energy landscape in the space around a selected plaquette for the area potential, U_A, volume potential, U_V, WCA potential of the triangle heights, U_h, and a nonlinear bending potential relating to the dihedral angles, U_ϕ. The changes in energy relative to the initial configuration of the mesh were plotted as a function of the central vertex coordinates of the green plaquette. In the left column, the energies were calculated for the vertex coordinates on the surface of a sphere, and in the right column, on a plane perpendicular to the surface (see Fig. 15). The color bar displays the energy values in the units of $k_BT = 2.49\varepsilon$. The area compressibility was set to $k_A = 5.12 \times 10^5 k_BT/l^2$, and the bulk modulus to $k_V = 1.6 \times 10^7 k_BT/l^3$. Each panel plots 320 × 320 pixels.

(all mesh edges lie under the surface), and the mobile vertex i is the central vertex of the green plaquette. We report ΔU for two $2d$ slices [Fig. 15 (right)]: panels in the left-hand side (l.h.s.) columns of Figs. 16–18 show the variation of ΔU over the surface of the represented sphere; panels in the r.h.s. columns of the figures show the variation of ΔU over a perpendicular plane containing $\boldsymbol{q}_i$ and the center of the sphere.

The energies associated with the area and the volume are only affected by changes in the area of the triangles that belong to the central plaquette. Figure 16, rows *a* and *b*, show the plots of the area and volume energies of the mesh. The area and volume of the initial configuration of the mesh were used as the values for the ground-state area (A_0) and volume values (V_0) in Eqs. (1) and (2). The total area and volume of the mesh change very slightly when the vertex is moving within the green plaquette (left panels), as confirmed by the measurements presented in Supplemental Material Fig. 6 [77].

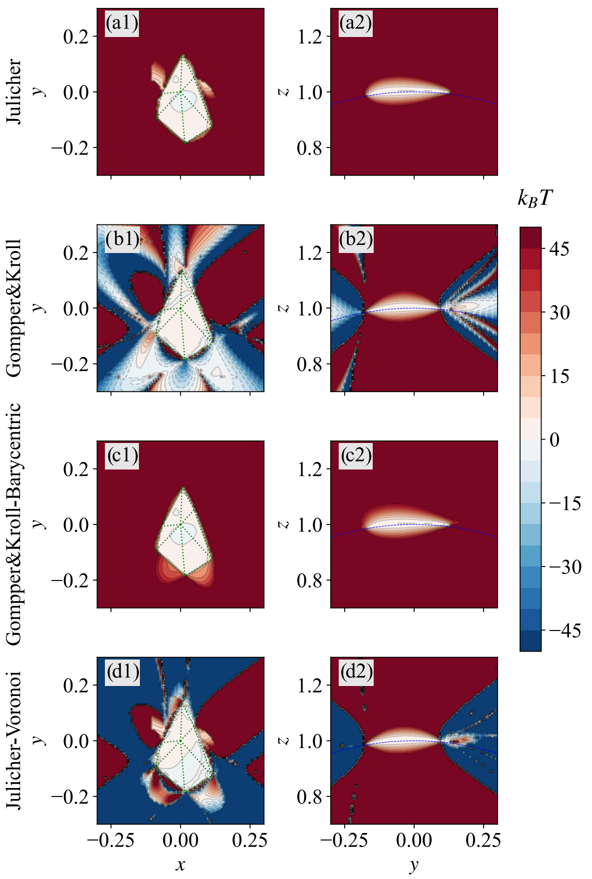

FIG. 17. The change in the mean curvature energy of a spherical mesh when the central vertex of a selected plaquette moves on the surface of the sphere (left column) or on a plane perpendicular to the surface (right column) while all other vertices are fixed in space. For all rows, the curvature energy difference was plotted relative to the initial configuration where the central vertex is at the origin of the xy plane. $\kappa = 20k_BT$. Each panel plots 320 × 320 pixels.

However, the area increases as soon as the vertex passes over an edge. The volume energy, however, only increases in the direction of the normal to the plaquette surface (right panel). Therefore, the motion of the vertex on the surface does not cost much in terms of the volume energy. The strengths of the area and volume energies depend on the area compressibility k_A, and the bulk modulus k_V, which are the material properties of the system. We have used $k_A = 5.12 \times 10^5 k_BT/l^2$ and $k_V = 1.6 \times 10^7 k_BT/l^3$ [88]. Figure 16 rows (c) and (d) plot two auxiliary potentials that do not have a physical origin but are tools that help stabilize the dynamics of the vertices. Row (c) plots the effect of the Weeks-Chandler-Anderson potential U_h on the triangle heights, and row (d) plots the effect of the nonlinear bending energy U_ϕ on the angle of the triangle pairs. U_h builds a wall around the edges (and consequently the vertices) and restricts the movement of the central vertex. U_ϕ only takes effect when large dihedral angles appear (for example, right before a vertex crosses over an edge), as observed in both columns. In these plots we have set $\epsilon = 4k_BT$ for the U_h, with $d_h/r_0 = 0.02$ and $\kappa_\phi = 20k_BT$, where $k_BT = 2.49\varepsilon$.

Changes in the energy landscape for the bending models are both a function of the coordinates of the green plaquette

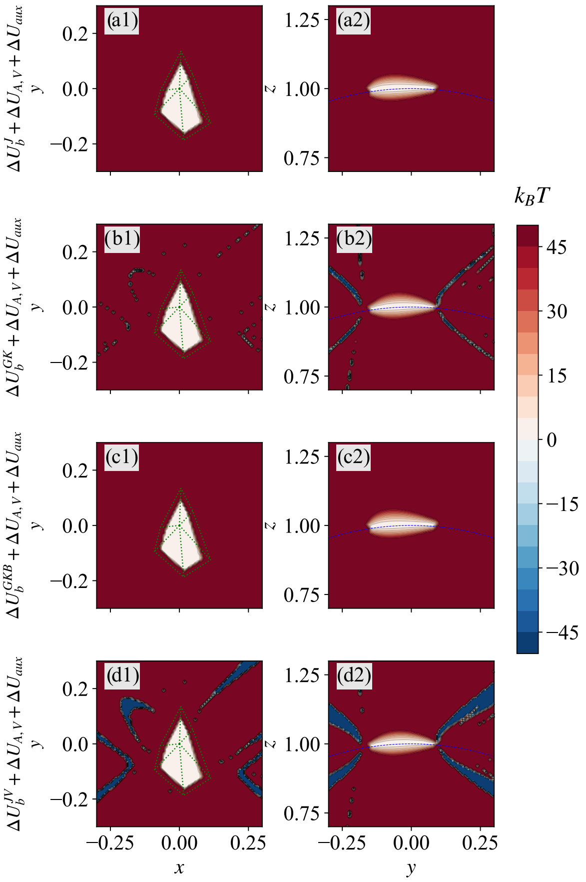

FIG. 18. Plots of the results presented in Fig. 17 after adding the area and volume energies and the two auxiliary potentials to each row. Not all numerical instabilities produced by the Voronoi calculations can be masked by the auxiliary potentials that make these models dynamically unstable. All parameters are set to the same values stated in Figs. 16 and 17. Each panel plots 320 × 320 pixels.

coordinates and its neighbors. Since the central vertex is also a member of the plaquettes indicated with orange edges in the left panel of Fig. 15, when its coordinates change, the angles (both dihedral and triangle angles) in its surrounding plaquettes are affected as well. In Fig. 17, the difference in the mean curvature energy of the mesh relative to the initial configuration was calculated for the four bending models. When the central vertex moves inside the green plaquette "zone" on the spherical cap (within an acceptable margin of error), the total mean curvature energy of the mesh does not change for either of the bending models. If the coordinate of the central vertex lies exactly on the plaquette edges or corner vertices, then the curvature energy calculations will break down since the definition of the angles of the dihedral and the triangle becomes ambiguous. It should be noted that since we chose to move the vertex on the sphere surface and not on the mesh, the coordinates will never lie precisely on the edges but will pass very closely over them. In other words, for the coordinates that lie outside the green plaquette, the left column shows how the energy landscape changes when the triangles begin to make folds on the surface, thus increasing the energy of the mesh. In the right column, for Voronoi-based models (Gompper&Kroll and Jülicher-Voronoi), a sudden drop in the mean curvature energy was observed when the plaquette made sharp angles (on both surfaces). This is due to sign changes in the Voronoi area calculations. Although the details of the energy landscape are functions of the green and orange plaquettes, the general behavior is the same for most configurations.

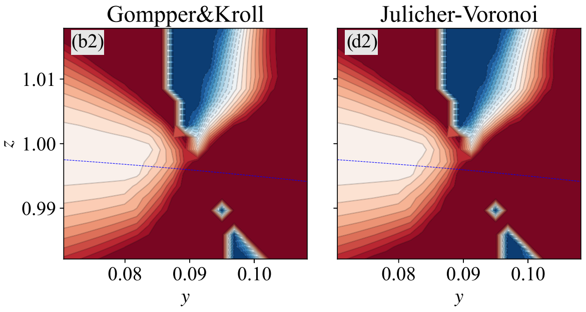

FIG. 19. A zoomed in version of the energy landscapes presented in Figs. 18(b2) and 18(d2) for the Gompper&Kroll and the Jülicher-Voronoi mean curvature models.

Figure 18 plots the energy landscape for the four bending models presented in Fig. 17 with the addition of the area and volume potentials and the two auxiliary potentials from Fig. 16. The mobile point can freely explore the target zone, a thin layer around the green plaquette sketched in Fig. 15, where its energy is essentially position independent. Within the target zone, we are back to the cases explored in Supplemental Material Fig. 6 [77] and Fig. 4. In particular, the choice of the expression for the discretized bending energy seems uncritical since near-identical results are obtained. Furthermore, the auxiliary potentials succeed in creating high energy barriers around the target zone. However, there is a fundamental difference between Voronoi- and Barycentric-based models when it comes to the energy profile outside the target zone and beyond the barrier.

For Barycentric-based models, i.e., the original Jülicher and the newly introduced Gompper&Kroll-Barycentric bending model, the mobile vertex will always be guided back to the target zone should an MD time step lead it outside. In fact, these models can recover from sharp bends and function without the nonlinear dihedral bending potential. In simulations involving drastic shape changes, we nevertheless recommend its use to prevent the formation of local artifacts.

In Voronoi-based models, the zones with large *negative* energies remain outside the target zone. Importantly, some of these regions are located just on the edge of the target zone where the Voronoi formula for the plaquette area changes sign. In particular, the close-up in Fig. 19 suggests the existence of low-energy transition paths out of the target zone that would allow a vertex to fall into one of these pitfalls and to disrupt the MD simulation via the accompanying conversion of potential into kinetic energy.

[1] B. Alberts, D. Bray, J. Lewis, M. Raff, K. Roberts, and J. Watson, *Molecular Biology of the Cell*, 4th ed. (Garland, New York, NY 2002)

[2] P. L. Yeagle, Chapter 1—Introduction, in *The Membranes of Cells*, 3rd ed., edited by P. L. Yeagle (Academic Press, Boston, MA, 2016), pp. 1–25.

[3] P. Canham, The minimum energy of bending as a possible explanation of the biconcave shape of the human red blood cell, J. Theor. Biol. **26**, 61 (1970).

[4] W. Helfrich, Elastic properties of lipid bilayers: Theory and possible experiments, Z. Naturforsch. C **28**, 693 (1973).

[5] D. Nelson and L. Peliti, Fluctuations in membranes with crystalline and hexatic order, J. Phys. France **48**, 1085 (1987).

[6] R. R. Lipowsky and E. E. Sackmann, *Structure and Dynamics of Membranes*, Handbook of Biological Physics; v. 1A (Elsevier Science, Amsterdam, 1995).

[7] G. Gompper and D. M. Kroll, Network models of fluid, hexatic, and polymerized membranes, J. Phys.: Condens. Matter **9**, 8795 (1997).

[8] R. Goetz, G. Gompper, and R. Lipowsky, Mobility and Elasticity of Self-Assembled Membranes, Phys. Rev. Lett. **82**, 221 (1999).

[9] H. Noguchi and M. Takasu, Self-assembly of amphiphiles into vesicles: A Brownian dynamics simulation, Phys. Rev. E **64**, 041913 (2001).

[10] J. C. Shillcock and R. Lipowsky, Equilibrium structure and lateral stress distribution of amphiphilic bilayers from dissipative particle dynamics simulations, J. Chem. Phys. **117**, 5048 (2002).

[11] S. Weinberg, *Statistical Mechanics of Membranes and Surfaces* (world Scientific, Singapore, 2004).

[12] H. Noguchi and G. Gompper, Dynamics of fluid vesicles in shear flow: Effect of membrane viscosity and thermal fluctuations, Phys. Rev. E **72**, 011901 (2005).

[13] R. Dimova and C. Marques, *The Giant Vesicle Book* (CRC Press, Taylor & Francis Group, Boca Raton, FL, 2019).

[14] D. P. Tieleman, S. J. Marrink, and H. J. C. Berendsen, A computer perspective of membranes: Molecular dynamics studies of lipid bilayer systems, Biochim. Biophys. Acta, Rev. Biomembr. **1331**, 235 (1997).

[15] A. J. Kox, J. P. J. Michels, and F. W. Wiegel, Simulation of a lipid monolayer using molecular dynamics, Nature (London) **287**, 317 (1980).

[16] P. van der Ploeg and H. J. C. Berendsen, Molecular dynamics simulation of a bilayer membrane, J. Chem. Phys. **76**, 3271 (1982).

[17] P. van der Ploeg and H. J. C. Berendsen, Molecular dynamics of a bilayer membrane, Mol. Phys. **49**, 233 (1983).

[18] E. Egberts and H. J. C. Berendsen, Molecular dynamics simulation of a smectic liquid crystal with atomic detail, J. Chem. Phys. **89**, 3718 (1988).

[19] H. Heller, M. Schaefer, and K. Schulten, Molecular dynamics simulation of a bilayer of 200 lipids in the gel and in the liquid crystal phase, J. Phys. Chem. **97**, 8343 (1993).

[20] K. R. Pandit and J. B. Klauda, Membrane models of *E. coli* containing cyclic moieties in the aliphatic lipid chain, Biochim. Biophys. Acta Biomembr. **1818**, 1205 (2012).

[21] G. Srinivas, D. E. Discher, and M. L. Klein, Self-assembly and properties of diblock copolymers by coarse-grain molecular dynamics, Nat. Mater. **3**, 638 (2004).

[22] I. R. Cooke and M. Deserno, Solvent-free model for self-assembling fluid bilayer membranes: Stabilization of the fluid phase based on broad attractive tail potentials, J. Chem. Phys. **123**, 224710 (2005).

[23] I. R. Cooke, K. Kremer, and M. Deserno, Tunable generic model for fluid bilayer membranes, Phys. Rev. E **72**, 011506 (2005).

[24] B. J. Reynwar, G. Illya, V. A. Harmandaris, M. M. Müller, K. Kremer, and M. Deserno, Aggregation and vesiculation of membrane proteins by curvature-mediated interactions, Nature (London) **447**, 461 (2007).

[25] T. Schindler, D. Kröner, and M. O. Steinhauser, On the dynamics of molecular self-assembly and the structural analysis of bilayer membranes using coarse-grained molecular dynamics simulations, Biochim. Biophys. Acta Biomembr. **1858**, 1955 (2016).

[26] S. J. Marrink and D. P. Tieleman, Perspective on the martini model, Chem. Soc. Rev. **42**, 6801 (2013).

[27] A. B. Poma, M. Chwastyk, and M. Cieplak, Polysaccharide–protein complexes in a coarse-grained model, J. Phys. Chem. B **119**, 12028 (2015).

[28] H. I. Ingólfsson, T. S. Carpenter, H. Bhatia, P.-T. Bremer, S. J. Marrink, and F. C. Lightstone, Computational lipidomics of the neuronal plasma membrane, Biophys. J. **113**, 2271 (2017).

[29] S. J. Marrink, V. Corradi, P. C. T. Souza, H. I. Ingólfsson, D. P. Tieleman, and M. S. P. Sansom, Computational modeling of realistic cell membranes, Chem. Rev. **119**, 6184 (2019).

[30] A. P. Thompson, H. M. Aktulga, R. Berger, D. S. Bolintineanu, W. M. Brown, P. S. Crozier, P. J. in 't Veld, A. Kohlmeyer, S. G. Moore, T. D. Nguyen, R. Shan, M. J. Stevens, J. Tranchida, C. Trott, and S. J. Plimpton, LAMMPS—A flexible simulation tool for particle-based materials modeling at the atomic, meso, and continuum scales, Comput. Phys. Commun. **271**, 108171 (2022).

[31] M. J. Abraham, T. Murtola, R. Schulz, S. Páll, J. C. Smith, B. Hess, and E. Lindahl, Gromacs: High performance molecular simulations through multilevel parallelism from laptops to supercomputers, SoftwareX **1-2**, 19 (2015).

[32] P. Eastman, J. Swails, J. D. Chodera, R. T. McGibbon, Y. Zhao, K. A. Beauchamp, L.-P. Wang, A. C. Simmonett, M. P. Harrigan, C. D. Stern, R. P. Wiewiora, B. R. Brooks, and V. S. Pande, Openmm 7: Rapid development of high performance algorithms for molecular dynamics, PLoS Comput. Biol. **13**, e1005659 (2017).

[33] E. A. Evans, Bending resistance and chemically induced moments in membrane bilayers, Biophys. J. **14**, 923 (1974).

[34] S. A. Safran, Fluctuations of spherical microemulsions, J. Chem. Phys. **78**, 2073 (1983).

[35] R. Lipowsky, The conformation of membranes, Nature (London) **349**, 475 (1991).

[36] L. Miao, U. Seifert, M. Wortis, and H.-G. Döbereiner, Budding transitions of fluid-bilayer vesicles: The effect of area-difference elasticity, Phys. Rev. E **49**, 5389 (1994).

[37] G. Lim H. W., M. Wortis, and R. Mukhopadhyay, Stomatocyte–discocyte–echinocyte sequence of the human red blood cell: Evidence for the bilayer–couple hypothesis from membrane mechanics, Proc. Natl. Acad. Sci. USA **99**, 16766 (2002).

[38] K. A. Brakke, The surface evolver, Exper. Math. **1**, 141 (1992).

[39] T. Kohyama, D. M. Kroll, and G. Gompper, Budding of crystalline domains in fluid membranes, Phys. Rev. E **68**, 061905 (2003).

[40] H. Noguchi and G. Gompper, Shape transitions of fluid vesicles and red blood cells in capillary flows, Proc. Natl. Acad. Sci. USA **102**, 14159 (2005).

[41] I. V. Pivkin and G. E. Karniadakis, Accurate Coarse-Grained Modeling of Red Blood Cells, Phys. Rev. Lett. **101**, 118105 (2008).

[42] T. Willmore, *Total Curvature in Riemannian Geometry*, Ellis Horwood Series in Mathematics and Its Applications (Ellis Horwood, Chichester, UK, 1982).

[43] B. Duplantier, Exact curvature energies of charged membranes of arbitrary shapes, Physica A **168**, 179 (1990).

[44] M. Schneider, J. Jenkins, and W. Webb, Thermal fluctuations of large quasi-spherical bimolecular phospholipid vesicles, Journal de Physique **45**, 1457 (1984).

[45] S. T. Milner and S. A. Safran, Dynamical fluctuations of droplet microemulsions and vesicles, Phys. Rev. A **36**, 4371 (1987).

[46] U. Seifert, Configurations of fluid membranes and vesicles, Adv. Phys. **46**, 13 (1997).

[47] U. Seifert, Fluid membranes in hydrodynamic flow fields: Formalism and an application to fluctuating quasispherical vesicles in shear flow, Eur. Phys. J. B **8**, 405 (1999).

[48] A. Yazdani and P. Bagchi, Three-dimensional numerical simulation of vesicle dynamics using a front-tracking method, Phys. Rev. E **85**, 056308 (2012).

[49] M. Kraus, W. Wintz, U. Seifert, and R. Lipowsky, Fluid Vesicles in Shear Flow, Phys. Rev. Lett. **77**, 3685 (1996).

[50] S. Sukumaran and U. Seifert, Influence of shear flow on vesicles near a wall: A numerical study, Phys. Rev. E **64**, 011916 (2001).

[51] S. Meßlinger, B. Schmidt, H. Noguchi, and G. Gompper, Dynamical regimes and hydrodynamic lift of viscous vesicles under shear, Phys. Rev. E **80**, 011901 (2009).

[52] J. Deschamps, V. Kantsler, E. Segre, and V. Steinberg, Dynamics of a vesicle in general flow, Proc. Natl. Acad. Sci. USA **106**, 11444 (2009).

[53] S. K. Veerapaneni, Y.-N. Young, P. M. Vlahovska, and J. Bławzdziewicz, Dynamics of a Compound Vesicle in Shear Flow, Phys. Rev. Lett. **106**, 158103 (2011).

[54] D. Abreu, M. Levant, V. Steinberg, and U. Seifert, Fluid vesicles in flow, Adv. Colloid Interface Sci. **208**, 129 (2014).

[55] Y.-G. Tao, I. O. Götze, and G. Gompper, Multiparticle collision dynamics modeling of viscoelastic fluids, J. Chem. Phys. **128**, 144902 (2008).

[56] A. Farnudi, T. Heydari, and M. Heidari, The virtual cell model: 2.0.2 (2022), doi:10.5281/zenodo.7486761.

[57] T. Heydari, M. Heidari, O. Mashinchian, M. Wojcik, K. Xu, M. J. Dalby, M. Mahmoudi, and M. R. Ejtehadi, Development of a virtual cell model to predict cell response to substrate topography, ACS Nano **11**, 9084 (2017).

[58] P. Abadi, J. Garbern, S. Behzadi, M. Hill, J. Tresbeck, T. Heydari, M. R. Ejtehadi, N. Ahmed, E. Copley, H. Aghaverdi, R. Lee, O. Farokhzad, and M. Mahmoudi, Engineering of mature human induced pluripotent stem cell-derived cardiomyocytes using substrates with multiscale topography, Adv. Funct. Mater. **28**, 1707378 (2018).

[59] Y. Kantor and D. R. Nelson, Crumpling Transition in Polymerized Membranes, Phys. Rev. Lett. **58**, 2774 (1987).

[60] F. F. Abraham, W. E. Rudge, and M. Plischke, Molecular Dynamics of Tethered Membranes, Phys. Rev. Lett. **62**, 1757 (1989).

[61] J. P. Hale, G. Marcelli, K. H. Parker, C. P. Winlove, and P. G. Petrov, Red blood cell thermal fluctuations: Comparison between experiment and molecular dynamics simulations, Soft Matter **5**, 3603 (2009).

[62] G. A. Vliegenthart and G. Gompper, Compression, crumpling, and collapse of spherical shells and capsules, New J. Phys. **13**, 045020 (2011).

[63] J. Paulose, G. A. Vliegenthart, G. Gompper, and D. R. Nelson, Fluctuating shells under pressure, Proc. Natl. Acad. Sci. USA **109**, 19551 (2012).

[64] N. M. Geekiyanage, M. A. Balanant, E. Sauret, S. Saha, R. Flower, C. T. Lim, and Y. Gu, A coarse-grained red blood cell membrane model to study stomatocyte-discocyte-echinocyte morphologies, PLoS ONE **14**, e0215447 (2019).

[65] C. Itzykson, Random geometry, lattices, and fields, in *Proceedings of the GIFT Seminar Jaca 85*, edited by J. Jabad, M. Asorey, A. Cruz (World Scientific, Singapore, 1986), pp. 130–188.

[66] Frank Jülicher, The morphology of vesicles of higher topological genus: Conformal degeneracy and conformal modes, J. Phys. II France **6**, 1797 (1996).

[67] N. Ramakrishnan, P. B. S. Kumar, and J. H. Ipsen, Modeling anisotropic elasticity of fluid membranes, Macromol. Theory Simul. **20**, 446 (2011).

[68] D. H. Boaland M. Rao, Scaling behavior of fluid membranes in three dimensions, Phys. Rev. A **45**, R6947 (1992).

[69] D. M. Krolland G. Gompper, The conformation of fluid membranes: Monte Carlo simulations, Science **255**, 968 (1992).

[70] F. Jülicherand R. Lipowsky, Domain-Induced Budding of Vesicles, Phys. Rev. Lett. **70**, 2964 (1993).

[71] Frank Jülicher, Udo Seifert, and Reinhard Lipowsky, Phase diagrams and shape transformations of toroidal vesicles, J. Phys. II France **3**, 1681 (1993).

[72] N. Ramakrishnan, P. B. Sunil Kumar, and J. H. Ipsen, Membrane-mediated aggregation of curvature-inducing nematogens and membrane tubulation, Biophys. J. **104**, 1018 (2013).

[73] T. Kohyamaand G. Gompper, Defect Scars on Flexible Surfaces with Crystalline Order, Phys. Rev. Lett. **98**, 198101 (2007).

[74] M. Laradjiand P. B. Sunil Kumar, Dynamics of Domain Growth in Self-Assembled Fluid Vesicles, Phys. Rev. Lett. **93**, 198105 (2004).

[75] J. Li, M. Dao, C. T. Lim, and S. Suresh, Spectrin-level modeling of the cytoskeleton and optical tweezers stretching of the erythrocyte, Biophys. J. **88**, 3707 (2005).

[76] H. Noguchiand G. Gompper, Meshless membrane model based on the moving least-squares method, Phys. Rev. E **73**, 021903 (2006).

[77] See Supplemental Material at http://link.aps.org/supplemental/10.1103/PhysRevE.108.015301 for movies and their description, energy potential implementation details, data acquisition, and additional figures and analysis.

[78] A. Solernou, B. S. Hanson, R. A. Richardson, R. Welch, D. J. Read, O. G. Harlen, and S. A. Harris, Fluctuating finite

element analysis: A continuum mechanics software tool for mesoscale simulation of biomolecules, PLoS Comput. Biol. **14**, e1005897 (2018).

[79] E. Kreyszig, *Differential Geometry*, Differential Geometry (Dover Publications, Mineola, NY, 1991).

[80] D. E. Discher, D. H. Boal, and S. K. Boey, Simulations of the erythrocyte cytoskeleton at large deformation. II. Micropipette aspiration, Biophys. J. **75**, 1584 (1998).

[81] R. Lipowsky, Spontaneous tubulation of membranes and vesicles reveals membrane tension generated by spontaneous curvature, Faraday Discuss. **161**, 305 (2013).

[82] M. P. Sheetzand S. J. Singer, Biological membranes as bilayer couples: A molecular mechanism of drug-erythrocyte interactions, Proc. Natl. Acad. Sci. USA **71**, 4457 (1974).

[83] T. T. Nguyen, R. F. Bruinsma, and W. M. Gelbart, Elasticity theory and shape transitions of viral shells, Phys. Rev. E **72**, 051923 (2005).

[84] G. Gompperand D.M. Kroll, Random surface discretizations and the renormalization of the bending rigidity, J. Phys. I France **6**, 1305 (1996).

[85] M. Plischkeand D. Boal, Absence of a crumpling transition in strongly self-avoiding tethered membranes, Phys. Rev. A **38**, 4943 (1988).

[86] Y. Kantorand K. Kremer, Excluded-volume interactions in tethered membranes, Phys. Rev. E **48**, 2490 (1993).

[87] Z. Zhang, X. Liu, K. Yan, M. E. Tuckerman, and J. Liu, Unified efficient thermostat scheme for the canonical ensemble with holonomic or isokinetic constraints via molecular dynamics, J. Phys. Chem. A **123**, 6056 (2019).

[88] H. R. Vutukuri, M. Hoore, C. Abaurrea-Velasco, L. van Buren, A. Dutto, T. Auth, D. A. Fedosov, G. Gompper, and J. Vermant, Active particles induce large shape deformations in giant lipid vesicles, Nature (London) **586**, 52 (2020).

[89] J. Lidmar, L. Mirny, and D. R. Nelson, Virus shapes and buckling transitions in spherical shells, Phys. Rev. E **68**, 051910 (2003).

[90] R. Auhl, R. Everaers, G. S. Grest, K. Kremer, and S. J. Plimpton, Equilibration of long chain polymer melts in computer simulations, J. Chem. Phys. **119**, 12718 (2003).

[91] C. S. Peskin, Flow patterns around heart valves: A numerical method, J. Comput. Phys. **10**, 252 (1972).

[92] P. D. Thomasand C. K. Lombard, Geometric conservation law and its application to flow computations on moving grids, AIAA J. **17**, 1030 (1979).

[93] J. A. Benek, J. L. Steger, F. C. Dougherty, and P. Buning, *Chimera: A Grid-Embedding Technique*, Technical report, Arnold Engineering Development Center, Arnold Air Force Station, Tennessee (1986).

[94] D. Drabik, M. Przybyło, G. Chodaczek, A. Iglič, and M. Langner, The modified fluorescence based vesicle fluctuation spectroscopy technique for determination of lipid bilayer bending properties, Biochimica et Biophysica Acta Biomembranes **1858**, 244 (2016).

[95] X. Bian, S. Litvinov, and P. Koumoutsakos, Bending models of lipid bilayer membranes: Spontaneous curvature and area-difference elasticity, Comput. Methods Appl. Mech. Eng. **359**, 112758 (2020).

[96] E. Fermi, J. Pasta, and S. Ulam, *Studies of nonlinear problems I, Los Alamos Report LA1940 (1955)* (University of Chicago Press, Chicago, IL, 1965), Vol. II.

[97] D. H. Boaland M. Rao, Topology changes in fluid membranes, Phys. Rev. A **46**, 3037 (1992).

[98] E. Quemener and M. Corvellec, Sidusthe solution for extreme deduplication of an operating system, Linux J. **2013**, 3 (2013).

[99] S. Ljunggrenand J. C. Eriksson, Shape fluctuations of spherical micelles, J. Chem. Soc., Faraday Trans. 2 **80**, 489 (1984).

[100] M. Meyer, M. Desbrun, P. Schröder, and A. H. Barr, Discrete differential-geometry operators for triangulated 2-manifolds, in *Visualization and Mathematics III*, edited by H.-C. Hegeand K. Polthier (Springer, Berlin, 2003), pp. 35–57.

[101] G. Thürrnerand C. A. Wüthrich, Computing vertex normals from polygonal facets, J. Graph. Tools **3**, 43 (1998).